Composite Structures 337 (2024) 118080

Contents lists available at ScienceDirect

Composite Structures

journal homepage: www.elsevier.com/locate/compstruct

Short-term behavior of glass fiber-polymer composite bending-active elastica beam under service load application

Tara Habibi [a], Landolf Rhode-Barbarigos [b], Thomas Keller [a,*]

[a] Composite Construction Laboratory (CCLab), École Polytechnique Fédérale de Lausanne (EPFL), Switzerland
[b] Department of Civil and Architectural Engineering, University of Miami, USA

ARTICLE INFO

Keywords:
Bending-active elastica beam
Fiber-polymer composites
Material failure
Snap-through buckling
Strain-based failure criterion

ABSTRACT

Bending-active elastica beam is a structural configuration that is based on the elastic deformation of an initially straight beam. This deformation occurs when horizontal displacements are applied to a sliding support, causing the beam to bend into an arched shape. Previous research has focused on the stability of small-scale bending-active structures, thus not considering material strength, which is crucial in real-scale applications and structural design. This paper investigates the short-term structural behavior of bending-active elastica beams using pultruded glass fiber-polymer composite profiles, as used in real-scale structures. A series of short-term bending and service load application experiments were performed considering different bending degrees and loading scenarios. These results were used to validate finite element modeling. They demonstrated that steeper bent beams experience material failure, while shallower ones exhibit snap-through buckling. Material failure initiates on the tensile side of the beams, with cracks initiating at locations of maximum curvature. Higher bending degrees and symmetric loading result in higher maximum loads than lower bending degrees and asymmetric loading. A strain-based failure criterion, which can serve for structural design, is derived.

1. Introduction

The term "bending-active" refers to load-bearing structures, composed of initially straight and planar members such as beams and membranes, which are transformed into curved shapes through elastic deformation [1]. In the case of beams, when horizontal displacements are applied to sliding supports to bend beams into arched shapes, the resulting elastic deformation is known as an "elastica curve", which represents the post-buckling shape of slender beams under axial compression. Such members offer the advantage of ease in transportation to construction sites and rapid assembly by bending the straight elements and securing them with cables or membranes [2].

Appropriate materials for bending-active structures typically comprise timber and fiber-polymer composites [3,4]. In the case of temporary structures, using bending-active systems enables the creation of cultural complexes, exhibition spaces and meeting halls, in response to a demand for stable cost-effective structures that may be quickly erected and dismantled, e.g., the Ephemeral Cathedral of Créteil in Paris, France [5]. However, in permanent bending-active structures, the sustained stresses imposed by the bending process can induce viscoelastic effects such as creep and relaxation in composite materials. Depending on the fiber type used, the material strength might be time-dependent and reduced due to creep rupture. It is therefore essential that viscoelastic effects be considered in structural verifications for permanent structures [2].

The term "bending-active" was first introduced in 2011 by the ITKE research group at the University of Stuttgart, mainly in the context of a form-finding strategy for load bearing structures based on systematic elastic deformation [6]. However, this specific structural concept had already been introduced as early as the 1960s and later examined, but under different terminologies, such as "buckled strut" and "prestressed arch" [7–9]. While the term "bending-active" gained widespread acceptance in research after 2011, its earlier scientific background is often ignored. Consequently, earlier findings and accomplishments have not been adequately addressed in recent works and have thus been partially duplicated.

These two almost independent phases of work - on "prestressed arch" and "bending-active" members - are thus analyzed to provide an overall view of the state of knowledge and how this state has evolved. As a result, the origins of the novelties are traced, and gaps in knowledge concerning the practical application in real-scale structures, such as buildings and bridges, are identified. The review particularly reveals a

* Corresponding author.
E-mail addresses: tara.habibi@epfl.ch (T. Habibi), landolfrb@miami.edu (L. Rhode-Barbarigos), thomas.keller@epfl.ch (T. Keller).

https://doi.org/10.1016/j.compstruct.2024.118080
Received 8 December 2023; Received in revised form 6 February 2024; Accepted 26 March 2024
Available online 27 March 2024

lack of reliable experimental data to validate numerical models for bending-active members. Existing results are not applicable for real-scale structures as they primarily focus on stability, thus neglecting material strength and failure process. This last point is particularly critical for the design of bending-active structures, whose ultimate limit state verification includes material strength.

The main body of the paper thus experimentally investigates the short-term structural behavior of composite bending-active elastica beams under point loads until failure. Two main sets of experiments were conducted using pultruded glass fiber-polymer composite flat profiles, as they are commonly used in real structures [10]. The first set involved short-term bending experiments, during which the profiles were bent until failure. In the second set, a short-term service load application was performed with the profiles initially bent to a specific degree and then subjected to a transverse point load until failure. Various geometric parameters and loading conditions were examined to establish a practical failure criterion based on observed failure modes. Additionally, finite element modeling was carried out based on the analysis and design methodology proposed in the authors' prior work with numerical results validated by experimental data. Consequently, this study focuses on the behavior of bending-active composite elastica beams under short-term service loads, enhancing the understanding of the failure behavior, and offering guidance for structural design.

2. From prestressed arch to bending-active elastica beam

Since the 1950s, considerable attention has been given in structural engineering to the stability of arch structures [11–16]. The common point in all these works was that the studied arches were built in the intended arched shape and had fixed supports; their denomination varied, i.e. "arch" or "curved beam" were used.

In 1965, Roodra performed experimental studies on various structural elements including a new type of arch, which was formed by the buckling of straight steel strips and denominated "buckled strut", in order to demonstrate and understand the effect of small imperfections on the buckling behavior of elastic structures [7]. The small-scale specimens were made of high strength steel, but the experimental setup was not explained in detail and the experimental data poorly reported.

A new term, "prestressed arch", was introduced for this type of "buckled strut" in 1968 in [8]. A clear definition of the term was given in 1970 by Huddleston [9]: "A different type of arch (or shell), formed by the buckling of a thin strut or plate into an arched curve before attaching it to its supports, resulting in a prestressed arch". Huddleston used this term in opposition to the term "rigid arches", which were directly built in the arched shape, and not bent into this shape. The term "non-prestressed arch'' will henceforth be used for "rigid arch'', i.e. for arches directly built in their intended shape, with fixed supports, which seems more appropriate.

In [9], Huddleston also studied the buckling and post buckling behavior of a prestressed arch in a two-dimensional space, using a numerical technique introduced before in [17]. The numerical results were compared with experimental results obtained on the model of a dome composed of four prestressed arches; the agreement was, however, not satisfactory. Huddleston attributed the differences to the asymmetric buckling restraint imposed by intersecting arches, resulting in the experimental model bearing a higher load than the numerical model. In the same year, Clifton investigated the buckling and post-buckling behavior of shallow prestressed circular arches under either uniform pressure or a central load using nonlinear equilibrium equations [18]. He mainly studied the effects of varying levels of either compressive or tensile prestress imposed on the arches. These prestress levels were, however, primarily considered from a mathematical perspective, i.e., the differentiation between compressive and tensile prestress was made by using different signs, and they were not practically implemented. Clifton concluded that the buckling load decreases with increasing compressive prestress and increases with increasing tensile prestress.

In 1977, Wolde-Tinsae and Huddleston introduced the term "prestressed dome," which they defined as a dome created by arranging prestressed arches through buckled struts [19]. The authors extended the aforementioned numerical technique to investigate the response of prestressed arches to both in-plane and out-of-plane loading in a three-dimensional space. However, analyzing three-dimensional stability proved to be challenging due to missing values for initial conditions, which complicated the solution with the available computational technology at that time. The numerical solution was thus not satisfactory. Huddleston refined the numerical approach by reducing unknowns of initial conditions to solve the spatial problem in [20]. Finally, in 1981, Wolde-Tinsae and Huddleston presented their numerical analysis method for studying the nonlinear elastic behavior of the prestressed dome in a three-dimensional space [21]. Their approach involved breaking the dome into pre-buckled arch segments, analyzing each with their numerical technique, and then reassembling them to reconstruct the dome. Additionally, they addressed the "long-term behavior" of the prestressed arch for the first time, recommending materials resistant to creep under sustained stresses, such as high strength steel.

Thompson and Hunt, in 1982, extended their own theoretical solution previously developed for non-prestressed arches, to analyze the buckling and post-buckling behavior of prestressed shallow arches subjected to point loads [22]. They derived formulas to calculate the buckling load and post-buckling path for non-prestressed and prestressed arches. A comparison of these formulas revealed a 25 % reduction in the buckling load for prestressed arches due to the adverse effect of prestress. They emphasized the need for further experimental work for validation of their theory.

In 1986, a finite element program was developed by Chini, to determine the weight under which prestressed domes buckle [23]. The program could predict both symmetrical and asymmetrical buckling loads, considering large displacements and rotations. For the validation of the program, in 1988, Chini and Wolde-Tinsae conducted small-scale experiments on prestressed arches in a centrifuge at NASA Goddard Space Flight Center [24]. They investigated seven aluminum prestressed arches, i.e., four prismatic ones with varying rise-to-span ratios and three tapered ones with different tapering ratios. All arches had a span of 502 mm, corresponding to the maximum centrifuge clearance. The swinging platform of the centrifuge was used to attach the prestressed arches, and their self-weight was increased through the acceleration of the centrifuge, which resulted in the deformation and buckling of the arches. The experimental results revealed asymmetrical buckling modes. It was shown that the buckling load of the prestressed arches was proportional to their rise-to-span ratios and increased by increasing the rise. The agreement between numerical and experimental results confirmed the validity of the algorithm and demonstrated the utility of the centrifuge utility for studying self-weight-related stability issues.

In a subsequent study, in 1988 [25], Chini and Wolde-Tinsae compared symmetrical and asymmetrical buckling in prestressed and non-prestressed arches with a rise-to-span ratio less than 0.35 under either concentrated or uniform loads, using a nonlinear finite element model (FEM). Results showed that prestress adversely affected the buckling load, with a stronger impact on asymmetrical buckling. They also compared non-prestressed arches with circular and elastica shapes and found no significant impact of the shape on the buckling load, except for steeper arches, where circular arches exhibited slightly higher buckling loads.

An experimental and analytical study was conducted by Pippard in 1990 on a prestressed arch formed from a highly tempered steel strip, subjected to a point load to investigate its instability modes [26]. It was demonstrated that as the point load increased, the crown of the arch descended, and for certain values of span and support angle, snapped vertically, which was denominated "symmetrical plunging" mode of instability. In other cases, especially with shallow arches, one side lifted while the other dropped, denominated "asymmetrical skewing" mode of

stability. The experimental and analytical results were consistent within the scope of the work.

In the early 1990s, the stability of prestressed sandwich arches gained attention and were investigated in several works, e.g. [27–32], which confirmed their applicability for large-span enclosures. An experimental study was carried out by Nelsen, Mirmiran and Wolde-Tinsae on five prestressed arches, including one with a single-layer aluminum section and four with sandwich composite sections (aluminum facings with balsa or oak core) [27,32]. The experimental results were presented as load versus deflection responses, showing snap-through buckling for the single-layer section arch and material failure for sandwich arches. The results revealed significant increases in the load-bearing capacity of the sandwich arches compared to the single-layer section arch. Later in 1993, they conducted a comparative analysis on the stability of prestressed arches with sandwich and homogeneous sections, using a self-developed FE computer program [28]. Their findings revealed that for prestressed sandwich arches, the buckling load and governing buckling mode were influenced by the relative thickness and shear modulus of the core layer. Additionally, the buckling loads of prestressed sandwich arches increased proportionally with the rise of the arch. It was noted that sandwich construction offered advantages for prestressed arches, as it reduced vulnerability to loading imperfections and lateral-torsional buckling.

In 2000, in continuation of the prior prestressed dome project, Ragavan and Amde (formerly known as Wolde-Tinsae) investigated the nonlinear buckling of cable-stiffened prestressed domes by FEM [33,34]. In these numerical studies, various prestressed domes, created by bending flat members made of high yield strength materials into arched shapes, were stiffened with circumferential cable loops, and subjected to central point loads. The modified systems effectively resisted loading imperfections by preventing side-sway buckling. Furthermore, the buckling load increased significantly by 216 %, 250 %, and 307 % for prestressed domes with two, three, and four cable loops respectively, compared to unstiffened domes. In 2001, a numerical investigation into prestressed arch behavior was conducted by Mirmiran et al., considering factors such as arch rise-to-span ratio ($\geqslant$0.5), section tapering, support and loading conditions [35]. Findings indicated that symmetric buckling point loads increased with arch steepness, while asymmetric buckling point loads reached a plateau near a rise-to-span ratio of 0.5. Clamped arches were more stable than pinned arches, and the least stable conditions occurred when a point load was applied within 12 % to 27 % of the span-length from the crown or when only three-quarters of the span carried a uniform load. In 2002, the same group investigated elasto-plastic buckling in prestressed arches using FEM [36]. The numerical study highlighted that, steeper arches generally exhibited greater stability within their elastic range; however, this effect was reduced as the prestress exceeded 55 % of the yield strength.

In 2011, Knippers et al. introduced the term “bending-active” in the context of form-finding in [4] to describe structures previously known as “prestressed arches” or “buckled struts”. However, the previously established knowledge concerning prestressed arches was not addressed in this work.

During the same period, the stability of elastic grid shells, formed through the elastic deformation of initially flat grids, was investigated in various studies, e.g. [37–40]. The prestressed arch phase was also overlooked, except [40], which referenced a limited number of related works. The primary emphasis of all studies lay in the examination of diverse numerical analysis techniques and influencing parameters affecting buckling loads, such as geometry, prestress level, support conditions, steepness ratios, and bracing systems. The studies indicated that while compression forces from the bending process had a noticeable destabilizing impact on prestressed arches, their effect on elastic grid shells remained limited.

In 2014, Lienhard in [1,3] explored the potential of “bending-active” for generating new structural forms through the construction of five case study structures. The study revealed that bending-active systems exhibited stress-stiffening effects and complex structural behaviors. Tensile stresses stabilized, and compressive stresses destabilized the systems. The scaling of the bending-active structure was possible when dead load was negligeable, and axial forces did not destabilize the system. Opposing requirements had to be considered in the design, i.e., the bending stiffness should not be too high to facilitate the bending, while the overall stiffness should be high enough to assure structural stability. Moreover, the need for and importance of establishing a unified approach to form-finding, structural analysis, and design was emphasized. Again, prestressed arches were not considered in this work.

Considering form-finding, which entails determining the final curved configuration, several research studies were performed (without referring to the prestressed arch phase), e.g., [41–44]. In 2015, a method was presented by Lazaro et al. in [41], based on force-density principles, for identifying balanced arrangements within planar bending-active structures. Schleicher et al. in [42], compared form-finding and form-conversion methods in the context of bending-active plate structures, discussing their advantages and disadvantages through three case studies. The interdependence of form and force was explored through the design of textile hybrid systems in [43], while the dynamic relaxation method was applied in [44] for form-finding and analysis of elastic grid-shells.

In 2017, Lazaro et al. in [45] evaluated the effectiveness of pinned bending-active arches under a central point load compared to non-prestressed arches using elliptic integrals. The results showed a buckling load reduction of less than 10 % in bending-active arches due to existing compressive axial forces. In 2021, Bessini et al. [46] introduced an analytical approach for designing a particular type of bending-active braced arch, utilizing a continuous flexible rod activated by lower cables and secondary struts. This method was tailored to a specific structural type and could not be applied more broadly.

In the authors’ prior study in 2022 [2], the feasibility of using fiber-polymer composites for permanent large-scale bending-active elastica beams was demonstrated. A systematic structural analysis and design methodology considering long-term viscoelastic effects and creep rupture was introduced and subsequently utilized in a parametric study. The study revealed that several key factors significantly affect the maximum load capacity: cross-section, straight beam length, type of composite material (glass, basalt, carbon), and bending degree, which defines the steepness of the beam in relation to the imposed sustained stress. To maximize the load bearing capacity, the bending degree should be increased until the creep rupture stress limit is approached. Furthermore, enhancing material stiffness and raising the creep rupture stress limit allowed for longer spans, higher load bearing capacity, and more efficient material use. As a result, for footbridge or roof applications, spans up to 30 m could be reached if using carbon fiber composites, while the spans were limited to 10 m for glass fiber composites, and the possible spans for basalt fiber composites fall in between.

Recently, in 2023, Xie et al in [36] conducted a study on the post-buckling behavior of composite bending-active arches. They performed central point loading experiments using thin carbon strips (48.5 $\times$ 1.4 mm in cross-section) with rise-to-span ratios ranging from 0.2 to 0.6. The experimental setup closely resembled the work of Pippard [26]. The study involved deriving and solving differential equations to describe the equilibrium path, validating analytical results with experimental data. The investigation revealed a reduction of approximately 10 % in the buckling load of composite bending-active arches when compared to those without prestresses, aligning with the results in [45]. The potential for scaling due to minimal gravity load was emphasized, as previously concluded in [1,3]. Furthermore, the study showed that increasing rise-to-span ratio increased the buckling load of composite bending-active arches due to higher curvature, as already found in previous studies.

From the above review it can be concluded that, despite the extensive research in prestressed arches and bending-active structures, there is a significant lack of reliable experimental data for validating the

numerous theoretical methods. Existing results tend to be limited in scope, are often poorly reported, or derived from small-scale structures. Moreover, most studies have focused on stability, particularly elastic buckling, thus not considering material strength. At the scale of buildings or bridges, however, structural failure of bending-active structures occurs when the bending strength of the material is exceeded, i.e., normally long before the buckling load is reached, and this critical aspect remains largely unexplored within the context of these studies. Furthermore, at real scale, the dead load cannot be neglected anymore and structures are thus not scalable.

3. Experimental program and modeling

To consider composite bending-active elastica beams as primary structural members, the short- and long-term structural behavior must be understood [2]. The sustained stresses (i.e., prestress) imposed by the bending process, and those caused by service load applications, must satisfy short-term structural safety and serviceability conditions, while, due to the viscoelastic nature of composites, long-term conditions must also be met [2]. The short-term structural behavior of composite bending-active elastica beams is investigated in this paper, both experimentally and numerically, in two consecutive steps, i.e., (1) the bending of the beam into an arched shape, and (2) the external service load application on the bent beam.

3.1. Experimental program

3.1.1. Material and specimen description

Pultruded glass fiber-composite flat profiles with a rectangular cross-section of 100 × 10 mm and straight length of 2400 mm were used. These profiles were composed of E-glass fibers embedded in an isophthalic polyester resin. The fiber architecture mainly consisted of unidirectional rovings in the central region and two combined mats in the outer regions; the corresponding fiber volume fraction by weight was 60 %. According to the manufacturer, the elastic modulus was 23 GPa, and the tensile, compressive and shear strength were 240, 240 and 25 MPa, respectively [47].

When the elastic modulus was fitted to the experimental results, the fitted values were consistently within 5 % of the provided value from the manufacturer. Consequently, 23 GPa was utilized in the numerical analysis.

3.1.2. Experimental setup and procedure

A fully automated experimental setup was designed to investigate two-pinned bending-active elastica beams, allowing profiles to be bent into targeted shapes and then loading them through a point load in the second step. The overall setup configuration is shown in Fig. 1. In the first step (bending process) a horizontal displacement denoted as W_X (up to 1800 mm) was applied to the sliding support (left side) via a cable, with a tensile force T. Each specific displacement value led to a pre-stressed elastica beam with a span of l, and a rise of f. In the second step (service load application) the elastica beam was subjected to an either symmetric or asymmetric point load labeled as P_S or P_A on its crown, again by applying a tensile force via a cable.

The setup included a marble platform with prefabricated holes that accommodated the installation of supports, and steel rails, which allowed the sliding support to move, see Figs. 2 and 3. The supports were each composed of three main mechanical steel parts, as shown in Fig. 3a: a box, a roller, and a base. The profile with dimensions of 100 × 10 mm was placed inside the box and secured using small bolts, see Fig. 3b (green color). The box was rigidly connected to rollers on each side, which could freely rotate in the surrounding fixed steel block. All these components were installed on the support base. The sliding and pinned supports were identical. The only difference was that the pinned support was fixed to the marble base, while the sliding support could move along the rail during the bending process and was subsequently fixed in place by fixation bolts. The free body diagram of all active forces at the support is also shown in Fig. 3b. The axial force F in the profile can be decomposed into vertical and horizontal reaction force components R_Z and R_X, considering support rotation θ_Y.

In the first step, the profile was initially positioned in a straight state, and connected to the supports, see Fig. 2a. A slight upward deformation was manually applied at mid-span at the beginning to initiate the bending process. A horizontal displacement was then applied to the

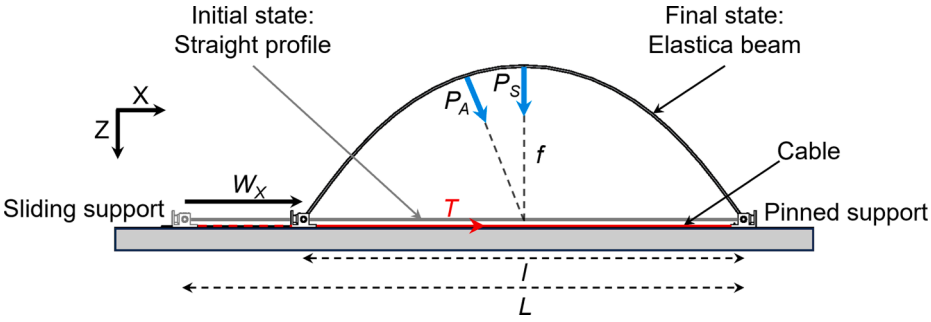

Fig. 1. Experimental setup configuration.

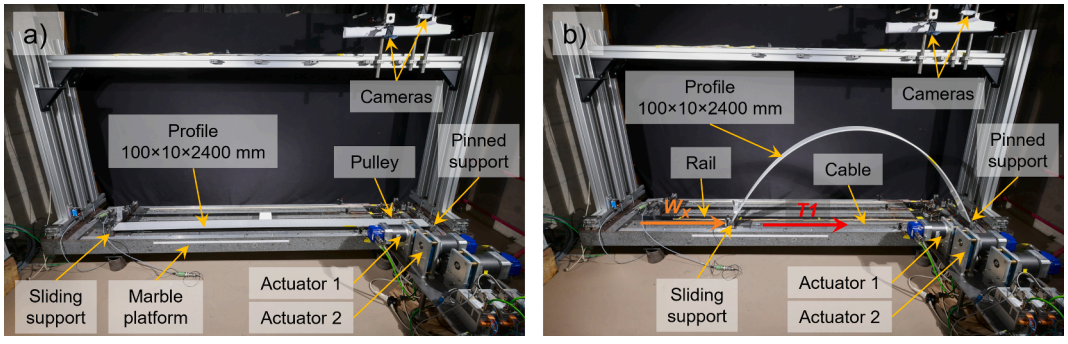

Fig. 2. Experimental setup for bending process, (a) initial state – straight profile; (b) final state – elastica beam.

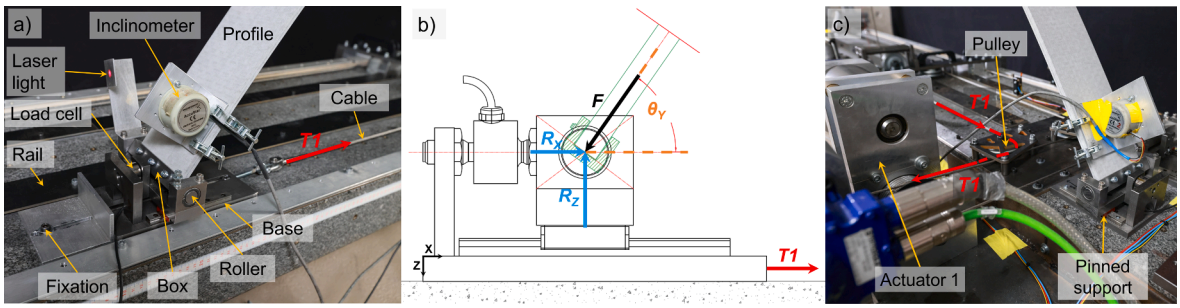

Fig. 3. Support configuration and instrumentation, (a) sliding support; (b) free body diagram at sliding support (black lines: side view; green lines: mid-section cut); (c) pinned support and pulley system to connect horizontal cable to actuator 1.

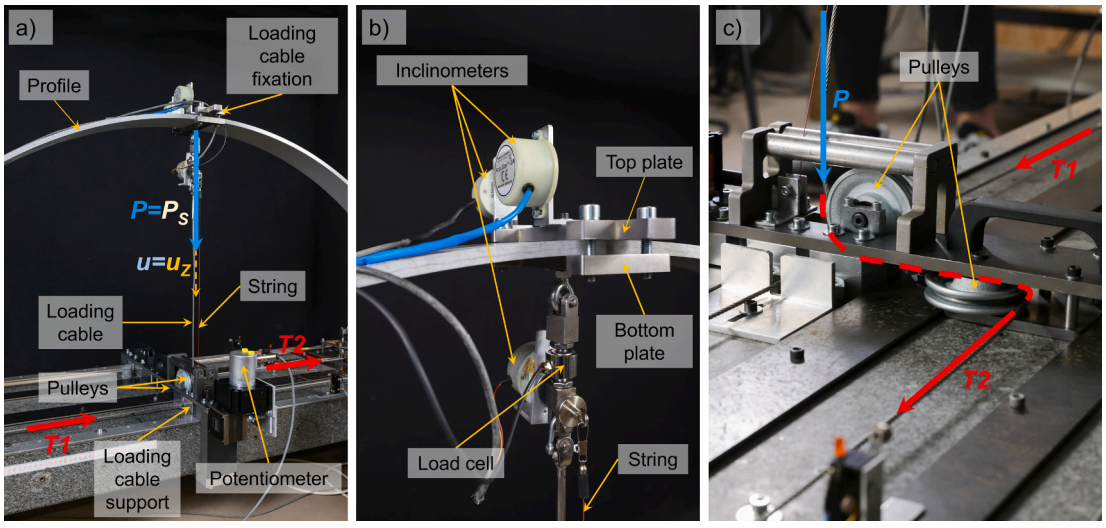

Fig. 4. Experimental setup for service load application and instrumentation, (a) setup overview for symmetric load application; (b) detail of loading cable fixation; (c) pulley system detail at loading cable support.

sliding support by pulling the cable ($T1$) with actuator 1 via a pulley, at a constant rate, until reaching the final state, i.e. the targeted elastica shape, see Figs. 2b and 3c. Subsequently, the sliding support was fixed to the platform.

In the second step, a displacement-control loading system was employed to apply a point load (P) to the prestressed elastica beam. Displacement control was selected to enable the tracking of crack initiation, failure process and softening behavior. This loading system, as shown in Fig. 4a, consisted of three main parts: a loading cable, its fixation, and support. One end of the loading cable was attached to the fixation system while the other end was attached to a support fixed onto the marble platform. The loading cable fixation was composed of two top and bottom steel plates bolted together, with the profile located in between, see Fig. 4b. The weight of loading cable fixation was 16 N and added to the measured point loads. A controlled vertical displacement u_Z was applied by pulling the loading cable down, at a constant rate, with actuator 2 (shown in Fig. 2), via a second pulley system ($T2$), see Figs. 4a and 4c.

For symmetric point load (P_S) application, the loading cable fixation was placed at the midspan, see Fig. 4a. For asymmetric point load (P_A) application, the loading cable fixation was positioned with an offset of $a = 200$ mm from the midspan with a rotating angle denoted as β, which was designed to decrease under the asymmetric deformation, and reach zero at the maximum load; thus $P_A = P \times \cos\beta$, and $u_Z = u \times \cos\beta$, see Fig. 5.

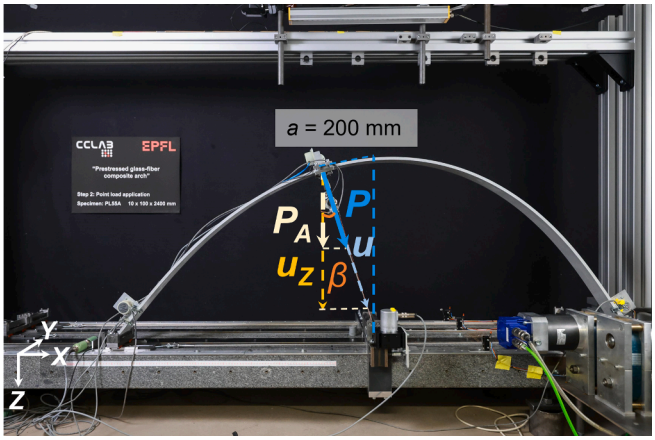

Fig. 5. Setup overview for asymmetric load application.

3.1.3. Instrumentation

During the experiments, the response of the elastica beam to the bending process and the service load application was measured using load cells, inclinometers, a laser distance sensor, strain gauges, and a string potentiometer. Additionally, two cameras were positioned on top of the specimen to record the experimental process, see Fig. 2. These cameras were used to capture visual information about the crack initiation on the top surface and subsequent failure process.

Horizontal support reaction forces (R_X) were measured using two load cells, while support rotations (θ_Y) were measured using two inclinometers, attached to both supports, with an accuracy of ± 2 N, and $\pm 0.02^\circ$ respectively, as shown in Fig. 3. A laser distance sensor with an accuracy of ± 1 mm was used to measure the applied horizontal displacements (W_X) on the sliding support, see Fig. 3a.

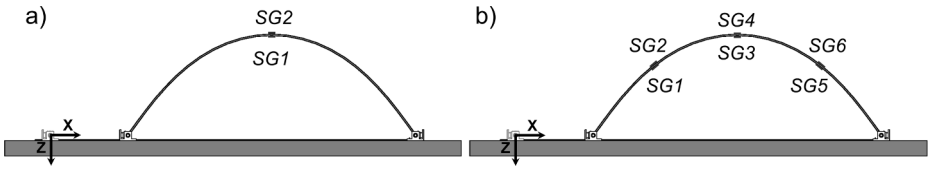

Fig. 6. Strain gauge plan, (a) short-term bending experiments; (b) short-term service load experiments.

The applied point load was captured by a load cell (±2 N accuracy) integrated into the loading cable, and the corresponding displacements were measured using a string potentiometer with an accuracy of ±2.5 mm, see Fig. 4a. Two inclinometers were also located on the loading cable fixation to measure possible in-plane and out-of-plane rotations during the loading process. A third inclinometer was used to measure the rotational angle of the loading cable, as shown in Fig. 4b.

Strain measurements were taken using electrical strain gauges on the glass profiles, positioned on the centerline of the top and bottom surfaces, see Fig. 6. The coordinates of the gauges varied in each experiment depending on the specific circumstances, described below. Among identical experiments, only one specimen was equipped with strain gauges.

3.1.4. Short-term bending experiments

The short-term bending experiments were conducted to examine the ultimate load, crack initiation and failure modes during bending, until failure occurred. Considering the viscoelasticity of the material, the effect of the (bending) displacement rate on the results was also investigated. Four rates ranging from 5 to 40 mm/s were thus selected, and three specimens were examined at each of the rates, which resulted in 12 experiments. For later use, among other things, the tensile stresses at crack initiation ($\sigma_{t,crack}$) were calculated.

3.1.5. Short-term service load experiments

The short-term service load experiments were performed to examine the maximum point loads under varying bending degrees (prestress levels). To achieve this, the profiles were bent at a constant (bending) displacement rate of 10 mm/s to a specific bending degree (prestress level, Step 1). Subsequently, the profiles were subjected to either symmetric or asymmetric point loads (P_S or P_A) in the transverse direction at a constant (loading) displacement rate of 1 mm/s until failure occurred (Step 2).

Four bending degrees were defined, corresponding to a bending of up to 45 %, 55 %, 65 %, and 75 % of the mean tensional stress at crack initiation ($\sigma_{t,crack,m}$), as obtained from the short-term bending experiments, where the bending degree at crack initiation is considered as 100 %. These bending degrees were obtained by applying W_X of 360, 510, 710, and 900 mm. Three specimens were examined at each of the selected bending degrees; the total number of experiments was thus 24.

To investigate the effect of the (loading) displacement rate on the results, four additional specimens with a bending degree of 55 % were examined under symmetric loading, at four rates ranging from 0.25 to 5.00 mm/s.

3.2. Numerical modeling

Structural analyses were carried out using the commercial Finite Element software Abaqus, which allows the simulation of large deformations and geometric nonlinearity. A 2D model was employed, utilizing B21 beam elements; each bending-active beam was represented by 200 elements, which were arranged in series along the beam axis. For each experiment, either a one-step structural analysis (for short-term bending experiments) or a two-step structural analysis (for short-term service load experiments) was employed comprising: (1) the bending process (Step 1), and (2) the service load application (Step 2).

In Step 1, the geometry of the straight simply supported beam was defined using two-dimensional space and beam elements with a very small point load of 2 N introduced at midspan to slightly uplift the straight profile and thus initiate buckling. The horizontal displacement was gradually applied to the sliding support using nonlinear large deformation static analysis. At the end of this first step, the targeted elastica beam was obtained.

In Step 2, the sliding support was fixed; the elastica beam thus comprised two pinned supports. The beam was then loaded considering the two service load cases (either symmetric or asymmetric). In both cases, the load was assumed to remain vertical during the analysis (see above). Due to the high degree of nonlinearity, the arc-length method was employed to capture the softening behavior while using load-control. This procedure involved incrementally applying a load to the structure, with the load increasing in small steps, and iteratively updating the solution until equilibrium was reached. The structural responses to the applied loading, i.e. the reaction forces, internal forces, strains, and nodal displacements, were obtained.

Concerning material properties, the elastic modulus was assumed as specified by the manufacturer (23 GPa). Due to the lightweight material, the weight of the beam was neglected. Modeling of material failure was not considered in order to obtain the full load versus displacement responses.

4. Experimental and numerical modeling results

The results obtained from the experimental and numerical investigations are summarized in Tables 1-4 and Figs. 7-20, and described in the following two subsections: 1) results of short-term bending experiments and modeling, and 2) results of short-term service load experiments and modeling. The comparison between the experimental and the numerical modeling results is also included in the following subsections, with the experimental results and numerical modeling results being denoted by *'Exp.'* And *'Mod.'* respectively, followed by the specimen designation.

4.1. Results of short-term bending experiments and modeling

The results of the short-term bending experiments and modeling are described in the following three subsections: (1) failure modes, (2) overview of experimental results and effect of (bending) displacement rate, and (3) comparison of experimental and modeling results. For each experiment, the specimen designation was created using the following format: the first term 'S' denotes short-term, the second term 'B' signifies the bending process, the subsequent numbers indicate the applied (bending) displacement rate, and the final character represents the specimen number with the same configuration.

4.1.1. Failure modes

All the investigated specimens failed on the tensile side of the elastica beam, as illustrated in Figs. 7 and 8. Small cracks initiated on the top surface in the crown region. These cracks then propagated across the surface. Shortly thereafter, the main crack opening occurred in the through-thickness direction, leading to subsequent progressive delamination in the middle layer of the profile, as shown in Figs. 7a and 8a. Additionally, a sort of wrinkling in the outermost polymer layer of the

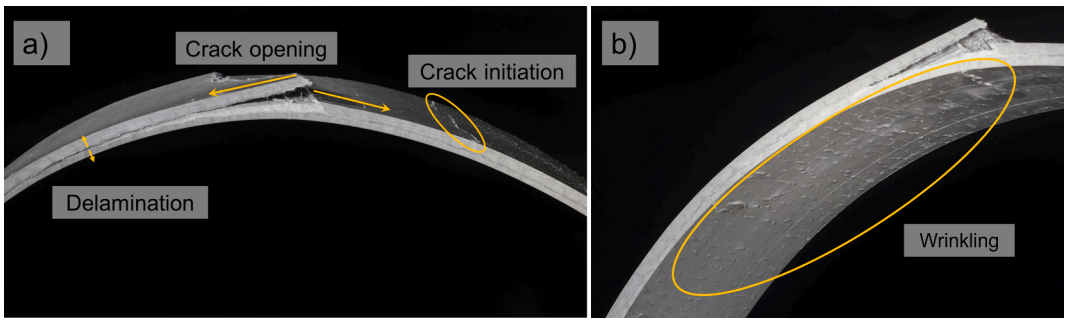

Fig. 7. Failure mode of short-term bending experiments, (a) cracks on crown top surface; (b) wrinkles on crown bottom surface.

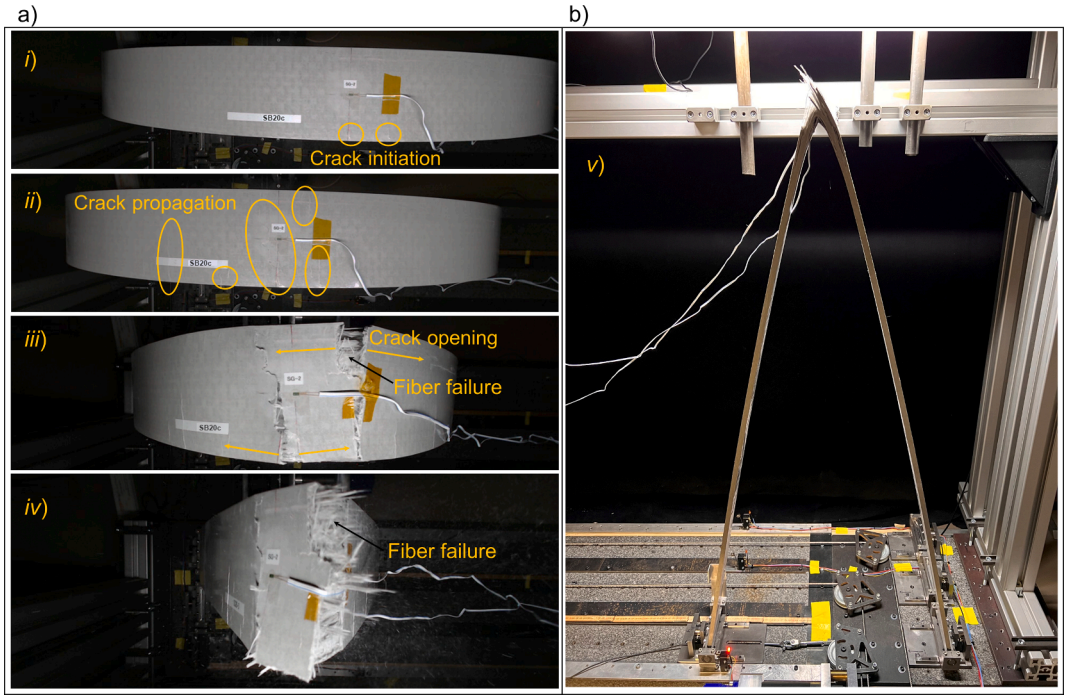

Fig. 8. Failure mode of *SB20c*, (a) crack initiation and propagation, and fiber failure (*i-iv*) on beam crown [top view]; (b) global view (*v*) at failure [side view].

profiles on the compressive side was observed, see Fig. 7b. The experiments were continued until the failure extended to fiber failure, as shown in Fig. 8.

4.1.2. Experimental results overview and effect of (bending) displacement rate

An overview of the short-term bending experiments conducted is provided in Table 1. The experimental results are categorized into two

Table 1
Overview of performed short-term bending experiments and results.

	Experimental results							Numerical results
		Crack initiation			Ultimate load			Crack initiation
Specimen designation	Bending displ. rate [mm/s]	$W_{X,crack}$ [mm]	$R_{X,crack,m}$ [N]	$\varepsilon_{t,crack}$ [%]	$W_{X,U}$ [mm]	$R_{X,U,m}$ [N]	$\varepsilon_{t,U}$ [%]	σ_t [MPa]
SB5a	5	1453	465	–	1681	495	–	260.1
SB5b	5	1451	460	–	1759	497	–	258.9
SB5c	5	1449	461	1.10	1783	506	1.18	258.3
SB10a	10	1450	457	–	1728	491	–	257.7
SB10b	10	1448	468	–	1789	505	–	263.0
SB10c	10	1504	475	1.08	1787	520	1.22	270.2
SB20a	20	1430	465	–	1718	498	–	255.2
SB20b	20	1402	459	–	1789	510	–	256.4
SB20c	20	1524	478	1.08	1787	520	1.23	272.0
SB40a	40	1464	466	–	1766	506	–	263.6
SB40b	40	1475	470	–	1789	518	–	257.0
SB40c	40	1557	482	1.14	1789	519	1.26	278.6
Mean		1467	467	1.10	1764	507	1.22	262.6
COV		0.028	0.017	0.026	0.020	0.020	0.027	0.028

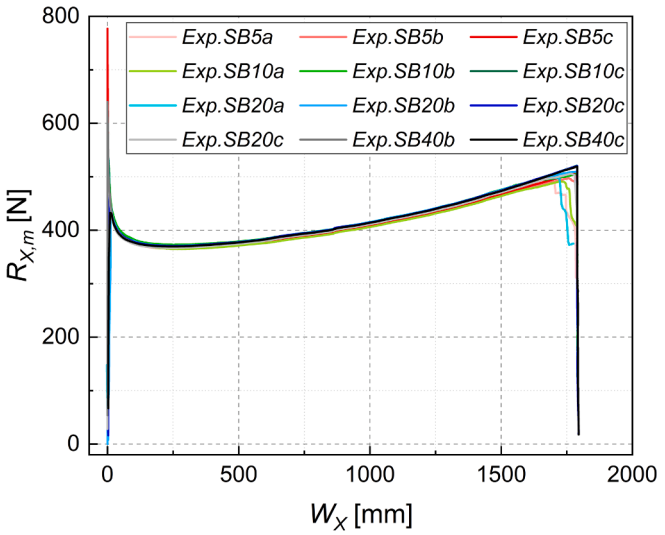

Fig. 9. Horizontal reaction forces (mean values) vs horizontal support displacements in short-term bending experiments.

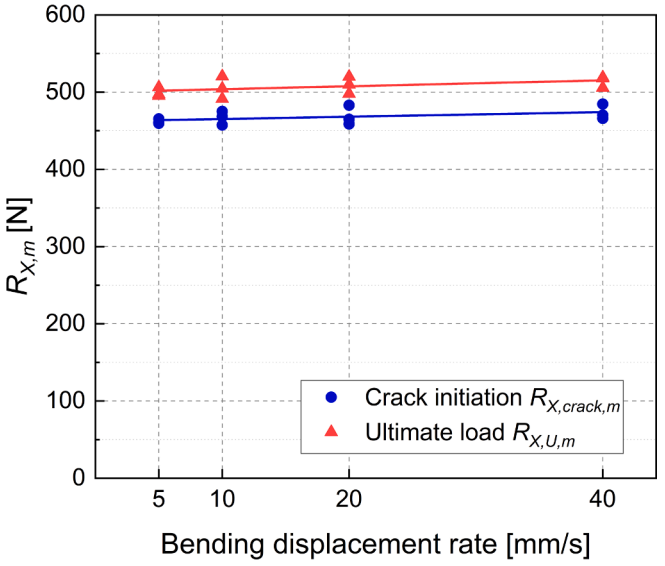

Fig. 10. (Bending) displacement rate effect on mean horizontal reaction forces in short-term bending experiments at crack initiation and ultimate load.

main sections: the structural responses when the first crack initiated; and when the ultimate load was attained. The numerical results are solely reported at the point of crack initiation, assuming the same $W_{X,crack}$ as obtained in the experiments. From the experimental responses, the horizontal displacements (W_X), the mean values of the two horizontal reaction forces ($R_{X,m}$), and the tensile strains (ε_t) on the crown top surface measured by the strain gauges (SG2), are reported. From the numerical responses, the tensile stresses (σ_t) at top surface of the crown are reported.

The calculated values of coefficients of variation (COV) of the different parameters reveal high consistency between measurements. The results also demonstrated that crack initiation consistently occurred at the same imposed displacement ($W_{X,crack}$) and stress level in the profile. This consistency can be extended to all other results such as horizontal reaction forces and strains as well.

The mean values of the measured horizontal reaction forces ($R_{X,m}$) versus applied horizontal displacement (W_X) of all examined specimens are shown in Fig. 9. In all curves, a sharp peak occurs at the beginning of the bending process, which is associated with the initial buckling of the specimen. Following that, a sudden drop in the reaction forces can be seen, followed by a gradual increase until failure. A significant scatter is manifested in the values of the initial peak, which is caused by the variation in the small manually applied uplift to the specimen at the beginning (see above). Subsequently, the results overlap, indicating that the change in (bending) displacement rate had no notable effect on the responses. This conclusion is also supported by the small values of COV reported in Table 1.

The effect of (bending) displacement rate on the mean horizontal reaction forces is further plotted at crack initiation and ultimate load in Fig. 10. Comparing the nearly horizontal lines in both confirms that the (bending) displacement rate had negligible influence on the structural responses ($R_{X,m}$). The parallel lines obtained for crack initiation and ultimate load indicate a proportional increase in reaction forces which proves the material remained completely elastic and did not show any viscoelastic behavior.

4.1.3. Comparison between experimental and numerical results

An example of the experimental and numerical responses obtained for a representative specimen, *SB20c*, is shown in Fig. 11. The measured and calculated horizontal reaction forces versus (1) the applied horizontal displacements, and (2) the axial strains at the beam crown, on the top and bottom surfaces, i.e., in tension and compression, are shown in Figs. 11a and 11b, respectively. The dash-dotted blue lines mark the crack initiation, and the stages of progressive failure (*i-iv*), which correspond to Fig. 8, are indicated. The experimental results are in good agreement with the modeling results until crack initiation. The aforementioned initial peak and drop of the horizontal reaction forces values are also visible in the strain gauge readings.

4.2. Results of short-term service load experiments and modeling

The results of the conducted short-term service load experiments and modeling are described in the following four subsections: 1) effect of (loading) displacement rate on maximum symmetric point load, 2) effect of bending degree on maximum symmetric and asymmetric point load, 3) failure modes under symmetric and asymmetric point load, and 4) comparison between the experimental and numerical modeling results. The specimen designation is as follows: the first term 'S' denotes short-term, the second term 'B' signifies the bending process, the subsequent numbers indicate the applied bending degree, followed by 'P' representing the point load application, then either 'S' or 'A' representing the symmetric or asymmetric loading case, and the final character represents the specimen number within the same configuration. In Section 4.2.1, the (loading) displacement rate value was further added to the specimen designation.

4.2.1. Effect of (loading) displacement rate on maximum symmetric point load

The effect of (loading) displacement rate on the maximum symmetric point load was investigated by conducting a series of experiments, as summarized in Table 2 and Fig. 12.

From the experimental responses, the maximum measured symmetric point load ($P_{S\max}$), and the corresponding vertical displacement at the beam crown ($u_{Z,P_{S\max}}$) are reported in Table 2. The corresponding COV values were small, again showing high consistency in the beam behavior. The load versus vertical displacement responses for all examined specimens are shown in Fig. 12. The results almost overlapped, demonstrating that the maximum point load is independent of the applied (loading) displacement rate.

4.2.2. Effect of bending degree

An overview of the short-term symmetric and asymmetric service load experiments performed is provided in Tables 3 and 4, respectively. In all conducted experiments, the (bending) and (loading) displacement rates in Step 1 and 2 were kept constant at 10 mm/s and 1.0 mm/s,

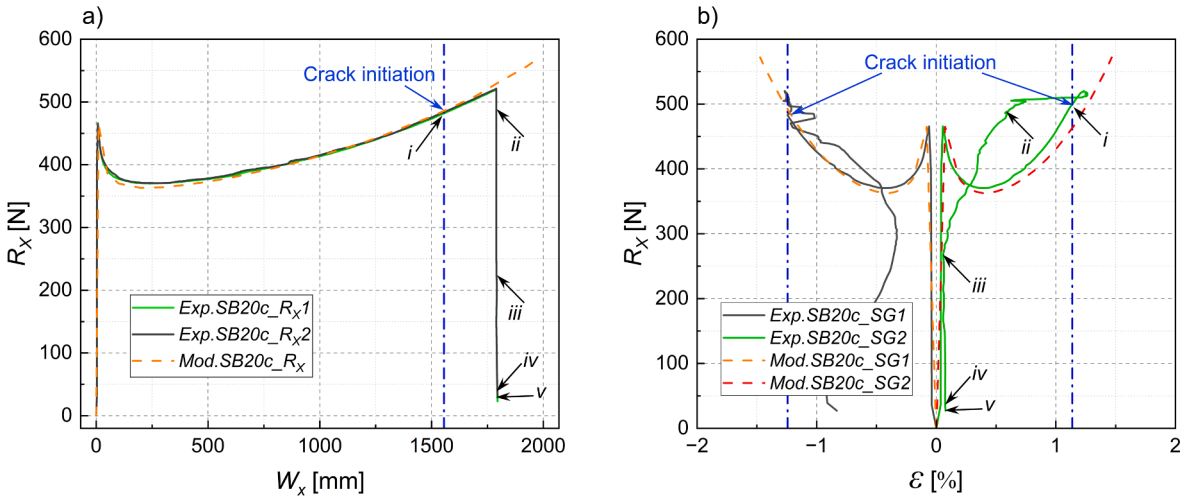

Fig. 11. Experimental and numerical results of *SB20c*, (a) horizontal reaction forces vs horizontal support displacements; (b) horizontal reaction forces vs axial strains at beam crown (blue dash-dotted lines indicate crack initiation).

Table 2
Overview of short-term service load experiments with different (loading) displacement rates and results.

Specimen denomination	Bending displ. Rate [mm/s]	W_X[mm]	Loading displ. Rate [mm/s]	P_{Smax} [N]	$u_{Z,P_{Smax}}$ [mm]
SB55PS0.25a	10	510	0.25	2077	260.5
SB55PS0.5a	10	510	0.50	2092	278.1
SB55PS1a	10	510	1.00	2133	276.2
SB55PS5a	10	510	5.00	2161	302.1
Mean				2116	279
COV				0.02	0.06

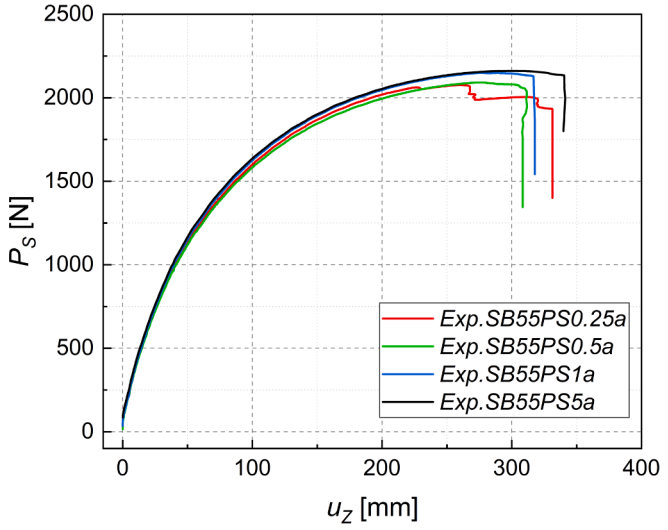

Fig. 12. Effect of (loading) displacement rate on maximum point load for *SB55PS* in short-term service load experiments.

respectively, while the bending degree was varied. The maximum measured symmetric point load (P_{Smax}), the corresponding vertical displacement ($u_{Z,P_{Smax}}$) at the beam crown, and the tensile strains at crack initiation ($\varepsilon_{t,crack}$), (measured by the strain gauges) are reported.

The load versus vertical displacement responses for all examined specimens are displayed in Fig. 13. The results indicate that, regardless of the loading case, the maximum point load increased with an increase in bending degree. Moreover, the initial stiffness of all specimens was almost identical. However, as the loading progressed, the specimens with higher bending degrees exhibited greater stiffness and failed at slightly lower displacement. Specimens bent to a bending degree of 45 % did not fail within the limits of the test setup; however, the plateau was reached, and a maximum point load was achieved. Crack initiation was captured using cameras located above the specimens and is indicated by dots on the curves. The results indicate that, in all specimens, crack initiation occurred before reaching the maximum load, with the exception of *SB55PA*, where the maximum load was reached a bit earlier (as discussed below). When comparing the symmetric and asymmetric load cases, regardless of bending degree, the maximum point load for the symmetric case is approximately double that of the asymmetric case.

4.2.3. Failure modes

Examples of typical symmetric and asymmetric failure modes are shown in Fig. 14 for specimens with 55 % bending degree. In all specimens, small cracks initiated on the top surface at the most curved location. They initiated symmetrically on both sides of the specimen in the case of symmetric loading, whereas in the asymmetric loading, they occurred on just one side. Subsequently, one crack opened, leading to progressive mid-thickness delamination. Additionally, wrinkles were observed in the outermost polymer layer on the compressive side. For all specimens, the failure extended to fiber failure except for the specimens loaded asymmetrically at a 55 % bending degree. Focusing on the global view, all specimens exhibited an asymmetric failure mode in the final stage. Even though the loading was entirely symmetric in the symmetric loading cases, the asymmetric propagation of cracks led to asymmetric failure in the end.

4.2.4. Comparison between experimental and numerical results

The comparison between experimental and numerical results is made for specimens bent to the lowest (45 %) and highest (75 %) bending degrees and subjected to both symmetric and asymmetric point loads. The process of applying service load to these specimens until failure is shown in Fig. 15. This process initiated after the bending to the specified degrees (phase *i*) and was followed by continuously applying the point load (phase *ii*), until failure occurred (phase *iii*). Specimens bent to a bending degree of 45 % (Figs. 15a and 15b) did not experience failure; they were bent up to the limits of the testing setup. However, as previously mentioned, a maximum in their load versus vertical displacement curves was reached.

Detailed results and comparison of structural responses are provided in the following two subsections: (1) bending process (Step 1), and (2)

Table 3
Overview of performed short-term symmetric service load experiments at (bending) and (loading) displacement rates of 10 and 1.0 mm/s and results.

Specimen denomination	W_X [mm]	Strain gauge X coordinates [mm]			$\varepsilon_{t,crack}$ [%]			P_{Smax} [N]	$u_{Z,P_{Smax}}$ [mm]
		SG1,2	SG3,4	SG5,6	SG 2	SG 3	SG 6		
SB45PSa	360	–	–	–	–	–	–	1775	243.9
SB45PSb	360	450	1150	1950	–	–	–	1768	245.2
SB45PSc	360	–	–	–	–	–	–	1808	244.7
SB55PSa	510	–	–	–	–	–	–	2149	276.2
SB55PSb	510	500	1150	1900	1.01	0.77	1.13	2118	280.7
SB55PSc	510	–	–	–	–	–	–	2164	275.2
SB65PSa	710	–	–	–	–	–	–	2479	268.7
SB65PSb	710	500	1150	1900	1.12	0.52	1.16	2451	249.9
SB65PSc	710	–	–	–	–	–	–	2464	238.8
SB75PSa	900	–	–	–	–	–	–	2620	254.8
SB75PSb	900	550	1150	1850	1.26	0.23	1.25	2538	215.2
SB75PSc	900	–	–	–	–	–	–	2457	205.9

Table 4
Overview of short-term asymmetric service load experiments performed at (bending) and (loading) displacement rates of 10 and 1.0 mm/s and results.

Specimen denomination	W_X [mm]	Strain gauge X coordinates [mm]			$\varepsilon_{t,crack}$ [%]			P_{Smax} [N]	$u_{Z,P_{Smax}}$ [mm]
		SG1,2	SG3,4	SG5,6	SG 1,2	SG 4	SG 6		
SB45PAa	360	450	1200	1950	–	–	–	771	186.7
SB45PAb	360	–	–	–	–	–	–	763	240.1
SB45PAc	360	–	–	–	–	–	–	751	239.2
SB55PAa	510	750	1200	1650	0.26	0.28	1.26	914	252.3
SB55PAb	510	–	–	–	–	–	–	922	247.3
SB55PAc	510	–	–	–	–	–	–	934	244.0
SB65PAa	710	750	1200	1650	0.08	0.45	1.10	1156	234.6
SB65PAb	710	–	–	–	–	–	–	1160	237.8
SB65PAc	710	–	–	–	–	–	–	1163	215.6
SB75PAa	900	650	1200	1750	0.33	0.63	1.15	1257	166.7
SB75PAb	900	–	–	–	–	–	–	1170	282.8
SB75PAc	900	–	–	–	–	–	–	1339	236.4

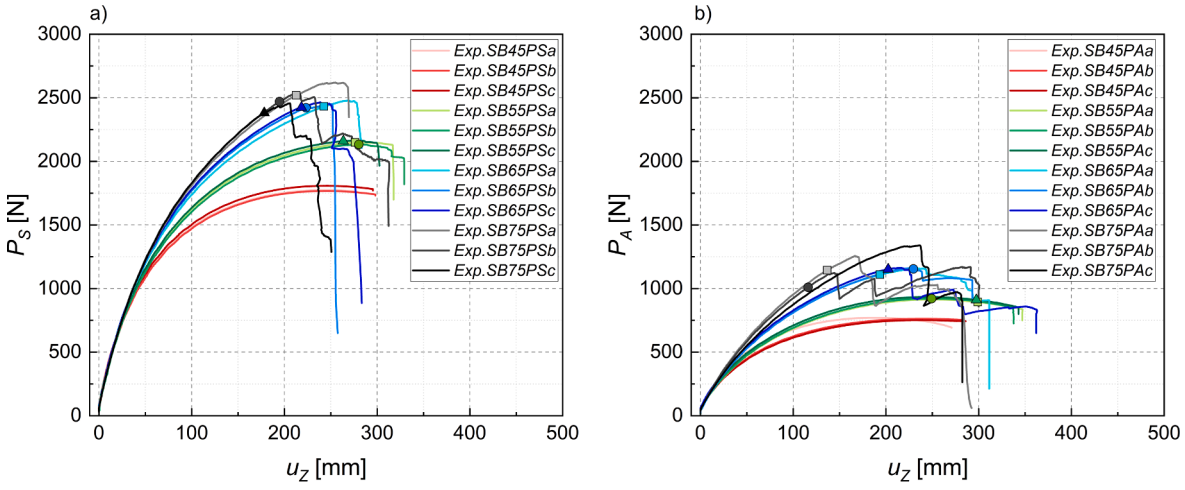

Fig. 13. Experimental load vs vertical displacement responses and points of crack initiation, (a) symmetric service load; (b) asymmetric service load.

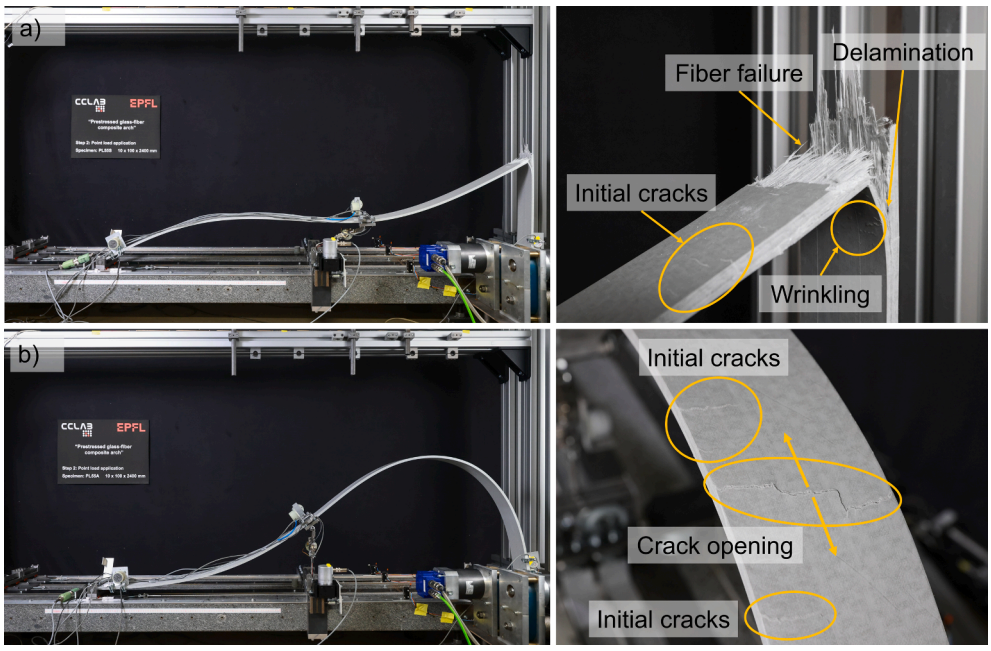

Fig. 14. Failure modes of service load experiments, global and local views (a) symmetric specimen *SB55PSc;* (b) asymmetric specimen *SB55Pac.*

service load application (Step 2). The difference between the results reported in Section 4.1 (short-term bending) and in the following description of the Step 1 bending process is that, in the former section, the beams were bent up to failure. However, in the following subsection, the beams are bent to a limited bending degree. It is necessary to model this bending process to consider the prestress level in the beam for further point load application.

4.2.4.1. Bending process (Step 1). An example of the experimental and numerical results obtained from the bending process of specimen *SB75PSb* is shown in Fig. 16. This specimen, with the highest bending degree, also includes the responses at lower bending degrees, marked with vertical blue dashed lines. The horizontal reaction forces, rotations at the supports, and strains at the locations of the strain gauges (defined in Fig. 6 and Table 3), are plotted against horizontal displacements in Figs. 16a-c, respectively. The comparison of numerical and experimental results shows good agreement.

When comparing the responses at highest (75 %) and lowest (45 %) bending degrees, all structural responses increased with higher bending degrees, i.e., the highest bending degree exhibited reaction forces 8 % higher than the lowest, as shown in Fig. 16a. The rotation of the two supports exhibited a highly symmetrical behavior during the bending process, confirming the effective functioning of the hinged supports, as shown in Fig. 16b. This symmetrical behavior is also represented in the strain curves when comparing the tensile and compressive strains, shown in Fig. 16c. Moreover, strains at the crown (*SG3* and *SG4*), were approximately twice as high as the strains measured at the sides (*SG1*, *SG2*, *SG5*, and *SG6*). This difference was slightly lower in the specimens with lower bending degrees.

4.2.4.2. Service load application (Step 2). Experimental and numerical results during service load application, for symmetric (*SB45PSb* and *SB75PSb*) and asymmetric (*SB45PAa* and *SB75PAa*) specimens, are compared in Figs. 17 to 20. The results again demonstrated good agreement between experimental and numerical results.

The load versus vertical displacement responses are displayed in Fig. 17. In the case of the least bent specimen (45 %), the theoretical and experimental behavior was identical in both loading cases due to the absence of material failure. However, for the specimens with the highest bending degree (75 %), the experimental and numerical curves started to deviate when crack initiation occurred, and, subsequently, the numerical maximum load exceeded the experimental load. Thus, in experiments, material failure occurred before reaching the maximum theoretical value. This divergence between experimental and theoretical maximum loads increased with the increasing of the bending degree.

The experimental and numerical load versus horizontal reaction force responses for both symmetric and asymmetric loading cases are plotted in Fig. 18. These curves started from the initial values of the horizontal reaction forces obtained from the bending process (Step 1), which is shown in Fig. 16a. As in previous results, the maximum theoretical point load in specimens with greater bending degrees exceeded that of the experiments. This difference decreased as the bending degree decreased.

The curves show that with higher bending degree, i.e. higher rise of the beam, the reaction forces decrease at the same load level, and, correspondingly, the axial forces in the beam also decrease (according to the free body diagram in Fig. 3b). The modeling curves reveal, furthermore, that the horizontal reaction forces, at the maximum theoretical load, remain constant and independent of the bending degree, for both symmetric and asymmetric loading cases.

The relationships between load and support rotation angle for both symmetric and asymmetric loading cases are shown in Fig. 19. The curves started with the initial values of the rotational supports obtained from the bending process (Step 1) shown in Fig. 16b. Experimental and numerical curves almost overlapped up to crack initiation, regardless of the loading case. For the symmetric case in Fig. 19a, the rotation of the two supports exhibited a highly symmetrical behavior before crack initiation, confirming the sustained symmetry of the applied loading. However, as can also be seen in Fig. 15c, after crack initiation, the asymmetric propagation of cracks on one side led to asymmetric failure. In the case of asymmetric loading, Fig. 19b, the rotation of the two supports exhibited asymmetrical responses throughout the loading process.

The experimental and numerical load versus strain responses for both symmetric and asymmetric loading cases are presented in Fig. 20. The initial strain values agree with those from the bending process (Step 1, Fig. 16c). As discussed before, the theoretical results of specimens bent to higher bending degrees exceeded the corresponding experimental results due to earlier material failure.

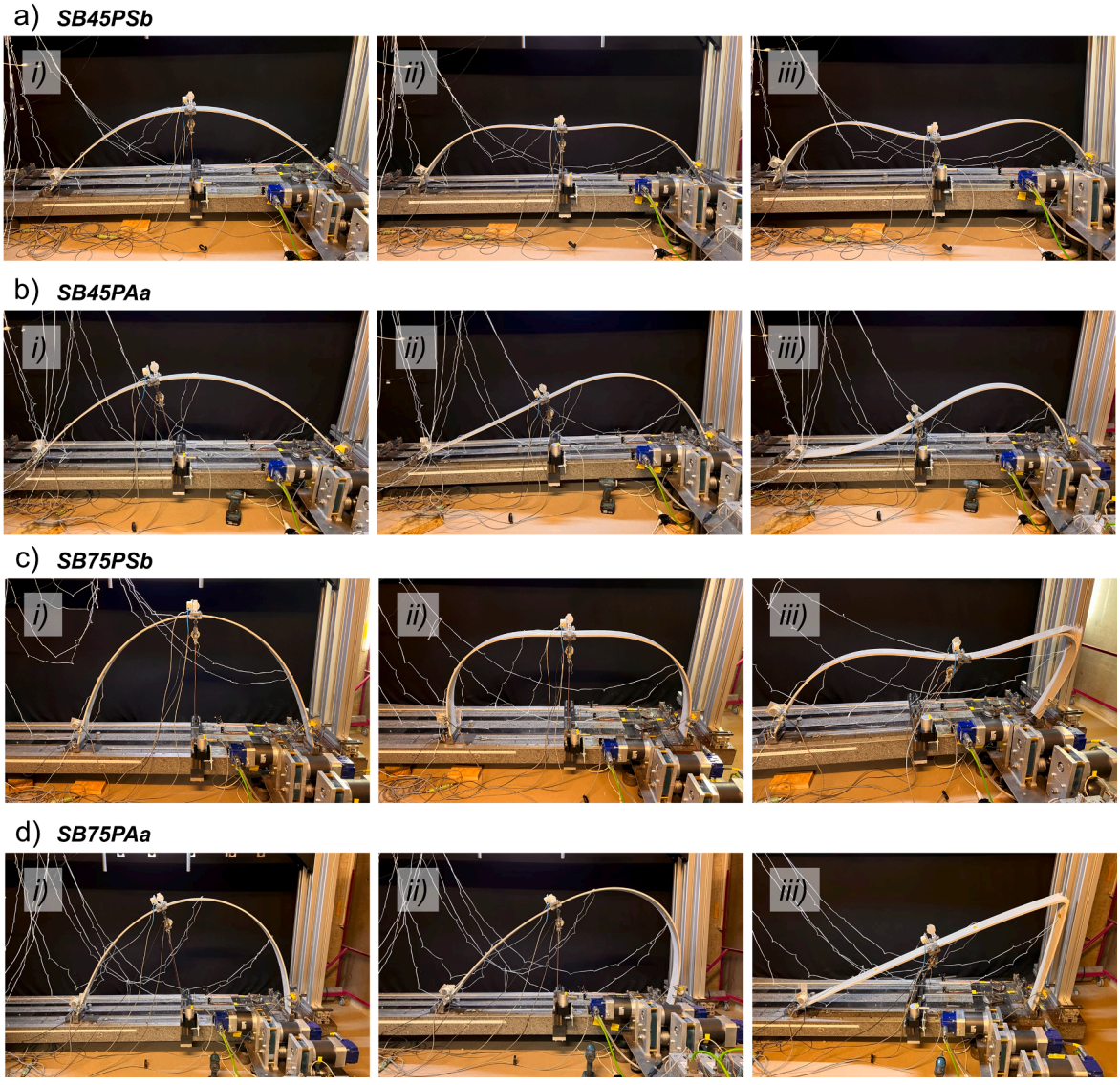

Fig. 15. Short-term load application process up to failure in phases *i) - iii)*, (a) symmetric load case *SB45PSb;* (b) asymmetric load case *SB45PAa; (c) symmetric load case SB75PSb; (d) asymmetric load case SB75PAa.*

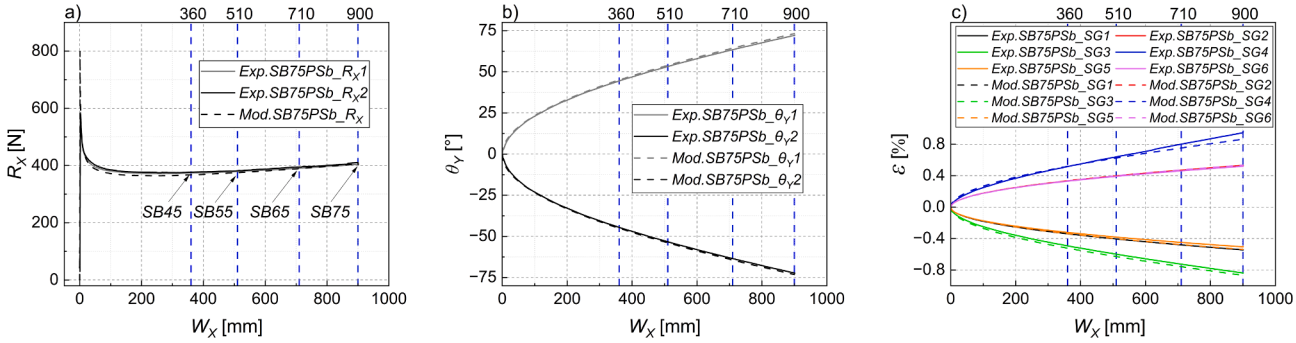

Fig. 16. Experimental and numerical results of *SB75PSb,* bending process, (a) horizontal reaction forces; (b) support rotations; (c) strains at specified strain gauge locations.

For the symmetrical load case, Fig. 20a, curves of *SG2* and *SG6* always overlapped, which confirmed the exact symmetrical behavior. Notably, the curves obtained from *SG4*, located at the mid-span, exhibited a shift in behavior from tensile to compressive strains as the loading progressed, due to the change in the curvature under the load. In the case of the asymmetrical load, as shown in Fig. 20b, the curves of *SG6* exhibited the highest tensile strains. This is attributed to the increased curvature on that specific side due to the asymmetry. Conversely, the strains reduced in the other gauge locations due to reduced curvature. A transition from tensile strains to compressive

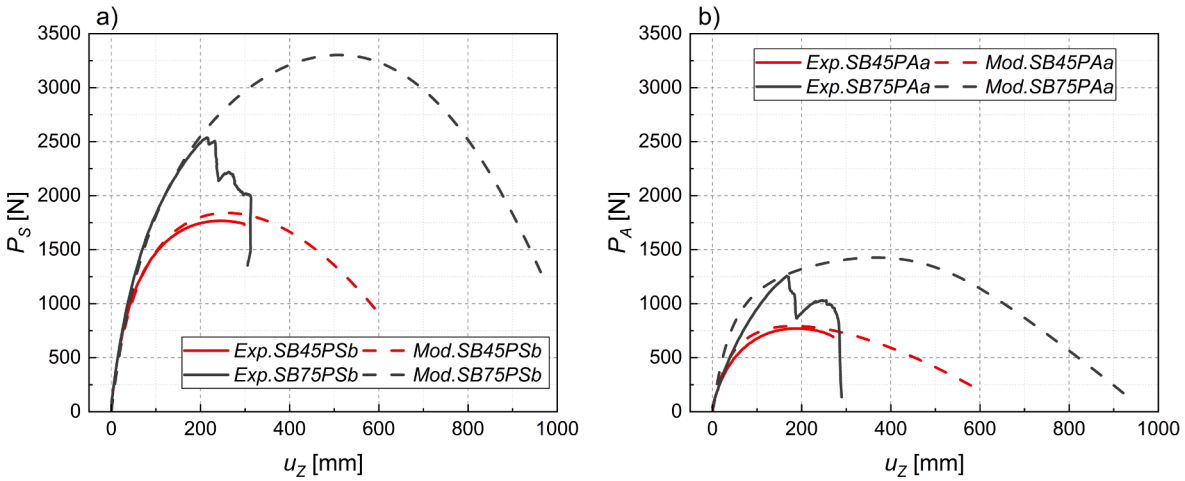

Fig. 17. Experimental and numerical load vs displacement responses at two bending degrees, (a) symmetric load cases *SB45PSb* & *SB75PSb*; (b) asymmetric load cases *SB45PAa* & *SB75PAa*.

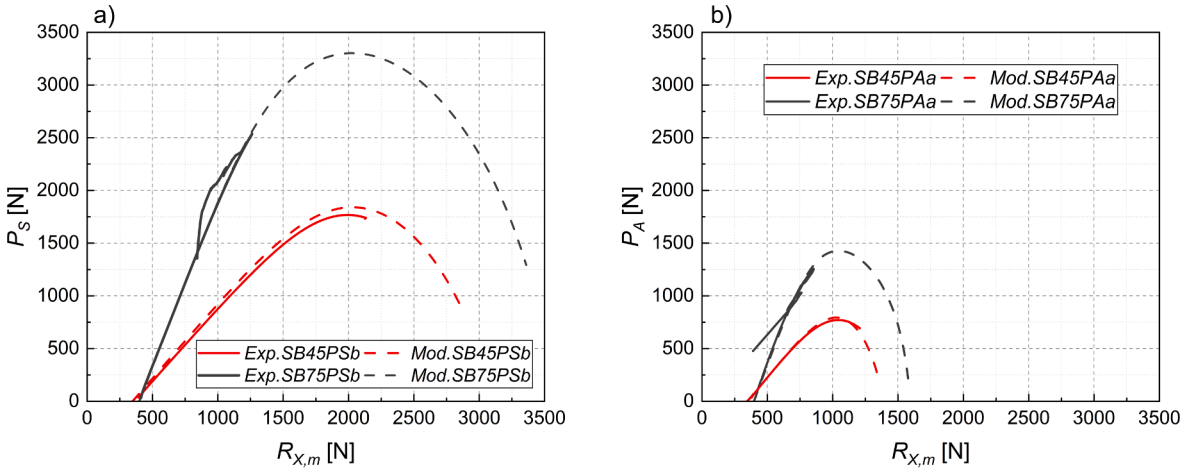

Fig. 18. Experimental and numerical load vs mean of horizontal reaction force responses, (a) symmetric load cases *SB45PSb* & *SB75PSb*; (b) asymmetric load cases *SB45PAa* & *SB75PAa*.

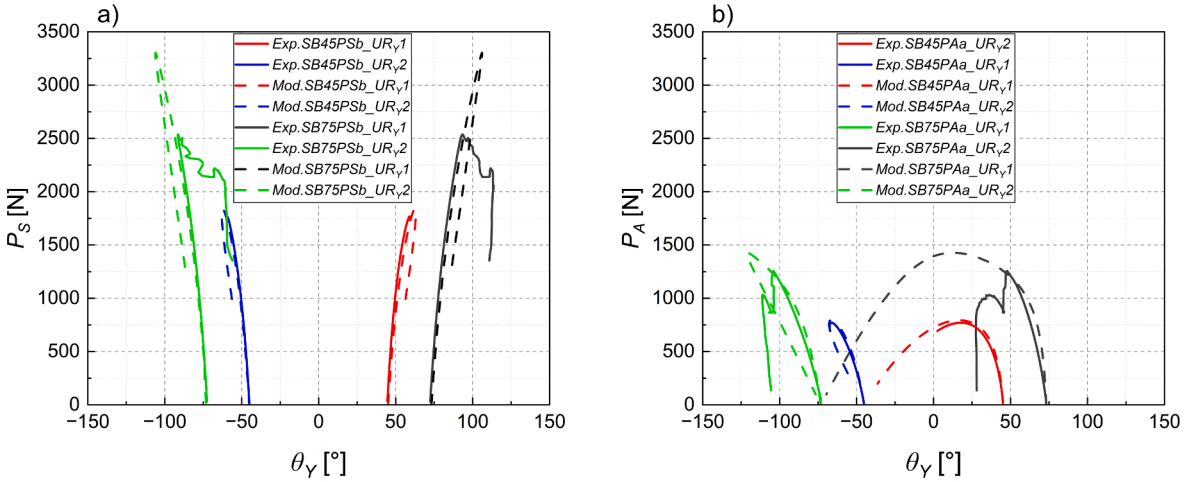

Fig. 19. Experimental and numerical load vs support rotation angle responses, (a) symmetric load cases *SB45PSb* & *SB75PSb*; (b) asymmetric load cases *SB45PAa* & *SB75PAa*.

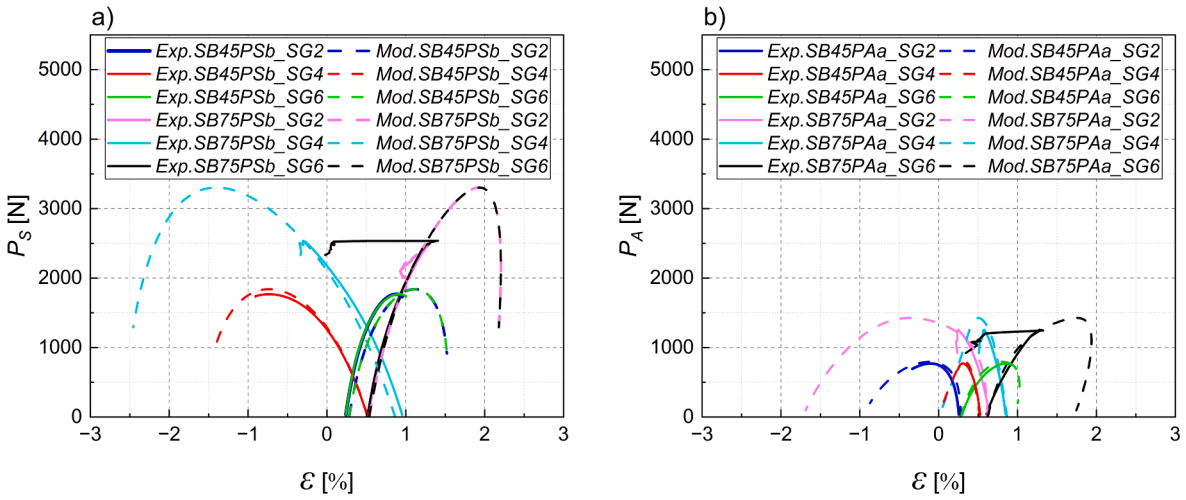

Fig. 20. Experimental and numerical load vs strain responses, (a) symmetric load cases *SB45PSb* & *SB75PSb*; (b) asymmetric load cases *SB45PAa* & *SB75PAa*.

strains was observable in the shallower specimen, while in the steeper one failure happened before this transition could occur.

The strains curves measured at the same locations, but with different bending degrees, were parallel before softening, indicating consistent stiffness of all specimens. This finding aligns with the results obtained from the load versus displacement responses displayed in Fig. 13.

5. Discussion

In this section, a detailed analysis of the sectional forces is presented to assist the understanding of the structural behavior and to identify the primary factors responsible for failure. Furthermore, the location of crack initiation in relation to the curvature is discussed, and a strain-based failure criterion is introduced.

5.1. Sectional forces and stresses

Numerical results for specimen *SB55PS,* which was bent to 55 % and then symmetrically loaded, were taken as a representative case to analyze the sectional forces. The corresponding diagrams are shown in Fig. 21 and are plotted in three phases: (1) at the completion of the bending process (end of Step 1), (2) at the load equivalent to the experimental load at crack initiation (P_{Scrack}), and (3) at the load equivalent to the maximum experimental load (P_{Smax}) during Step 2.

Concerning the first phase, the bending of the profile activated axial forces (compression) in the elastica beam, in addition to bending moments and shear forces. The corresponding maximum stress values are 0.37 MPa for axial stress, 0.43 MPa for shear stress, and 141.6 MPa for flexural stress. The axial stress is thus negligibly small compared to the flexural stress, while the latter amounts to approximately 60 % of the strength (240 MPa). The shear stress is also negligible compared to the shear strength (25 MPa).

When comparing the bending phase with the crack initiation and maximum load phases under symmetric load, a noticeable increase in all forces occurs, especially in axial forces (a fivefold increase), consequently leading to an increase in all stress levels, i.e. the maximum stress values at P_{Scrack}(P_{Smax}) are 1.85 (2.10), 1.72 (2.24), and 230.8 (284.2) MPa for axial, shear and flexural stresses, respectively. Although both axial and shear stresses have experienced notable increases, they remain negligibly small. The critical section of the beam also shifted from mid-span in the bending phase to approximately a quarter span in the loading phase, with a slight shift towards the supports in the latter case as the load increased.

It is clear from this analysis that flexural stresses dominate, and elastica beams subjected to point loads typically fail due to bending by exceeding the material bending strength. As the bending degree increases, flexural stresses also increase, ultimately leading to material failure. Conversely, in shallower specimens, i.e., those bent to a degree of 45 %, flexural stresses do not reach the material strength at the maximum load, which results in a snap-through buckling.

5.2. Curvature

Since curvature is the second derivative of the bending moment, it attains its maximum value where the moments and associated flexural stresses are at their peak. Consequently, it is expected that crack initiation occurs at the location with the highest curvature. This relationship is further investigated in this section with experimental and numerical

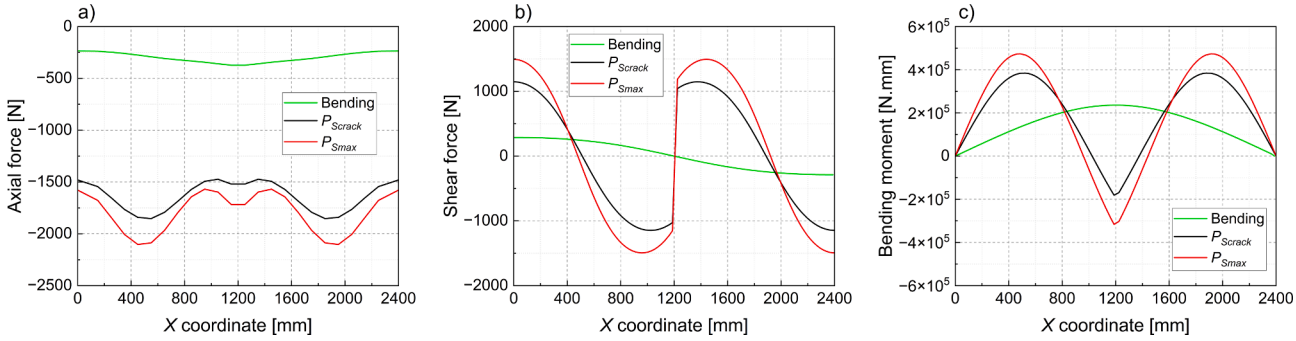

Fig. 21. Numerical results for sectional forces of *SB55PS* (under symmetric loading), at end of bending (Step 1), crack initiation (P_{Scrack}), and maximum experimental load (P_{Smax}), (a) axial forces; (b) shear forces; (c) bending moments.

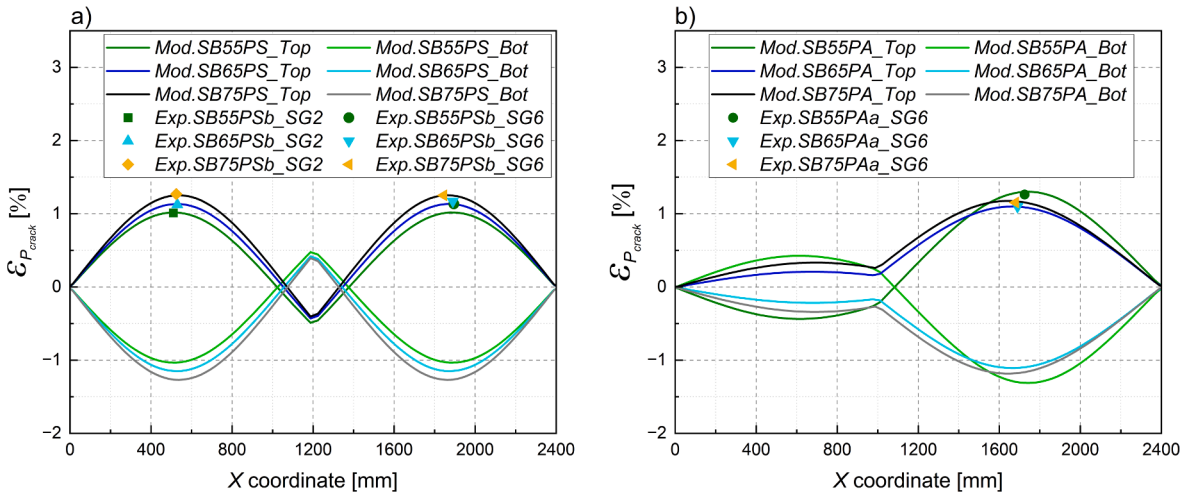

Fig. 22. Experimental ('Exp.') and numerical ('Mod.') strain values at crack initiation load along profile length, (a) symmetrical load cases; (b) asymmetrical load cases.

results for specimens bent to 55 %, 65 % and 75 % analyzed in this respect. In contrast to the preceding section, specimens with a bending degree of 45 % were not considered, since no crack initiation occurred.

The numerical strain paths along the length of the specimens, on the top and bottom surfaces and at the experimental crack initiation load ($\varepsilon_{P_{crack}}$) are shown in Fig. 22. The experimental locations where cracks initiated are shown as dots on the curves. As can be seen, regardless of bending degree or loading case, cracks always initiated at locations where the tensile strains were highest. These locations are approximately at both quarter spans for symmetric loading, see Fig. 22a, while in the case of asymmetric loading, they occur at just one quarter span, see Fig. 22b.

For further comprehension of the location of crack initiation, curvature values at the crack initiation load ($C_{P_{crack}}$) along the length of the specimens were calculated and presented in Fig. 23. The experimental crack locations are shown as dots on the curves. As evidenced by the graphs, regardless of the loading case (Fig. 23a for symmetrical and Fig. 23b for asymmetrical loading cases), cracks consistently initiated at locations of highest curvature.

Regarding the numerical results of the beam bent to 55 %, the curvature exhibits a change in sign at the load application point (Fig. 23b), which corresponds to the change of sign of the strains at the crack initiation load in Fig. 22b. This change occurs due to crack initiation immediately after reaching the maximum load, as was also mentioned in Section 4.2.2.

5.3. Strain-based failure criterion and failure mode

When designing structural members, the establishment of a failure criterion is required to prevent material failure. As crack initiation consistently occurs near the maximum load (Fig. 13), and strains at crack initiation were measured, the option of establishing a strain-based failure criterion is investigated in this section.

The effect of the bending degree on the experimental tensile strains at crack initiation ($\varepsilon_{t,crack}$) is shown in Fig. 24a. The mean value ($\varepsilon_{t,crack,m}$) is indicated by a green dash-dotted line. Regardless of the experimental type (symmetric or asymmetric loading, and bending degrees from 55 % to 100 %), the experimental data shows a consistency with small deviations from the mean. This result confirms that crack initiation depends on material properties and remains independent of the experimental type and bending degree. A "strain-based failure criterion" can thus be applied for the strength verification in design.

Since resistance values in design codes are characteristic values, i.e., 5 % fractile values [48], the characteristic value of the tensile strain at crack initiation is derived below. The characteristic value ($\varepsilon_{t,crack,k}$) was calculated according to prEN 1990:2021, Annex C, Eq. (C.15) [49]:

$$\varepsilon_{t,crack,k} = \varepsilon_{t,crack,m} \times \exp\{-k_n \times \sqrt{\ln(1+V_{\exp}^2)} - \frac{\ln}{2}(1+V_{\exp}^2)\} (1)$$

where $\varepsilon_{t,crack,m} = 1.14\%$, $V_{\exp} = 0.068$ (COV), and $k_n = 1.85$ for 13 results.

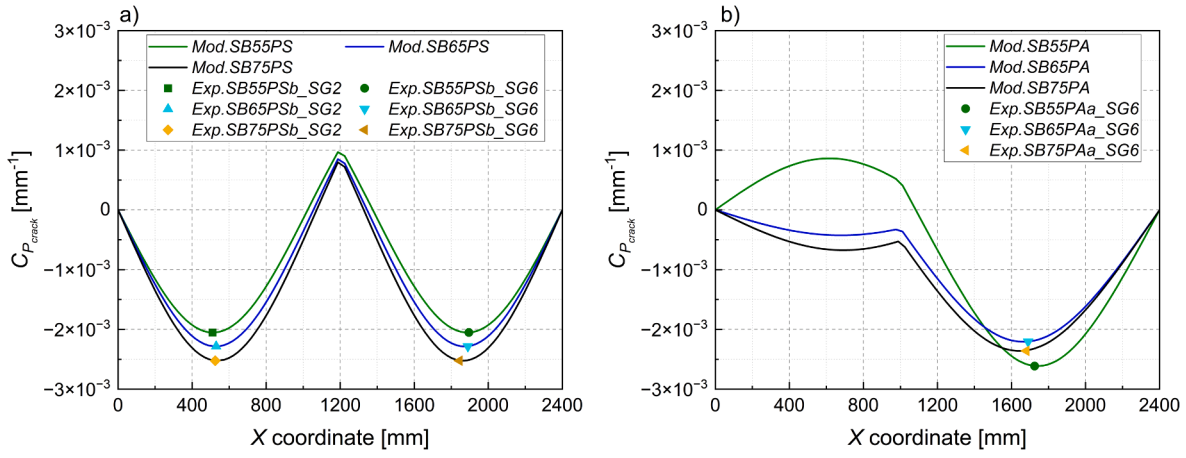

Fig. 23. Experimental and numerical curvature values at crack initiation load along the profile length, (a) symmetrical load cases; (b) asymmetrical load cases.

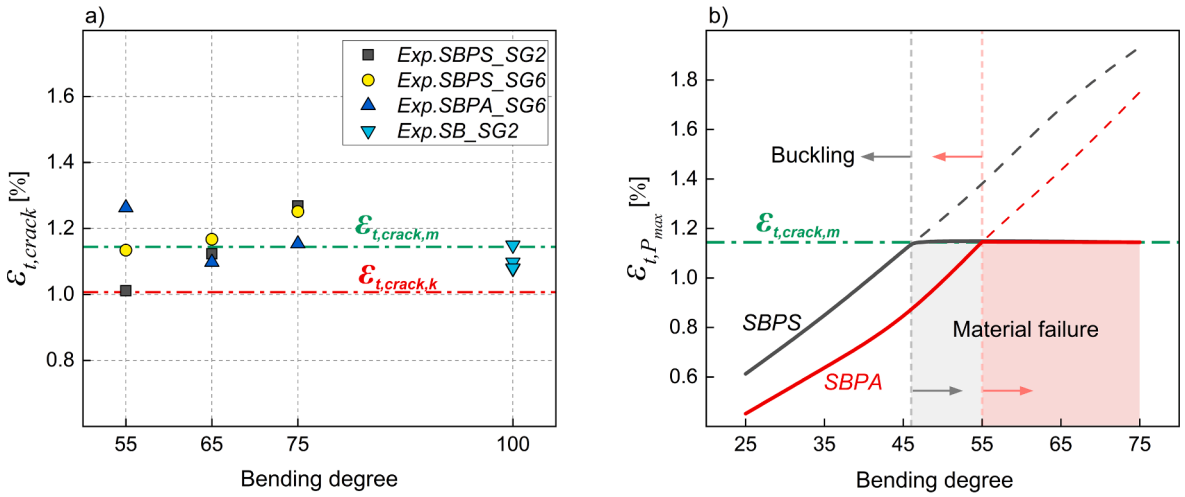

Fig. 24. Effect of bending degree on experimental and numerical tensile strains, (a) at crack initiation, (b) at maximum load (mean and characteristic values of experimental tensile strain at crack initiation shown in green and red dash-dotted lines, respectively).

The resulting characteristic value is $\varepsilon_{t,crack,k} = 1.01\%$, which is also shown by a red dash-dotted line in the Fig. 24a. This value can be used as a failure criterion in practical use in the design of this type of material.

The effect of the bending degree on the tensile strains at maximum load ($\varepsilon_{t,P_{max}}$) was further investigated numerically and is illustrated in Fig. 24b. Bending degrees ranging from 25 % to 75 % were considered for both symmetric (*SBPS*) and asymmetric load (*SBPA*) cases. The mean value of experimental tensile strains at crack initiation $\varepsilon_{t,crack,m}$ is also shown by a green dash-dotted line. Examining the continuous lines for *SBPS* and *SBPA*, reveals that specimens with a bending degree less than 45 % for symmetric loading and less than 55 % for asymmetric loading cases exhibit tensile strains at the maximum load that are below the mean strain at crack initiation. Consequently, these specimens do not fail due to material strength; instead, they experience a sudden collapse, i.e. snap-through buckling.

Specimens with bending degrees higher than 45 % for symmetric and 55 % for asymmetric loading exceed the mean strain at crack initiation at the point of maximum load. In such cases, material failure occurs before reaching the theoretical maximum load, as indicated by the dashed lines for each loading case in Fig. 24b.

6. Conclusions

An experimental and numerical investigation of a medium-scale bending-active elastica beam was conducted, involving two main load scenarios: the short-term bending process and the short-term service load application. In the bending process, the profiles were bent until failure occurred, while during the service load application, the profiles were bent to a specific bending degree and then subjected to a transverse symmetric or asymmetric point load until failure. The investigation considered various parameters, including (bending and loading) displacement rates, bending degree, symmetrical and asymmetrical loading cases. The following conclusions were derived:

(1) The analysis demonstrates that steeper beams experience material failure under service load application, while shallower beams undergo a sudden collapse known as snap-through buckling.
(2) The results of service load application experiments indicate that beams with a higher bending degree, i.e. higher rise, exhibited higher maximum point loads, but lower horizontal reaction forces.
(3) Beams under symmetric load cases always show significantly higher maximum point loads than those under asymmetric load cases.
(4) In both short-term bending and service load application experiments, in steeper beams, crack initiation occurs on the tension side at locations of maximum curvature. The cracks subsequently propagate through the thickness and lead to delamination in the mid-plane of the profiles. Ultimately failure occurs through fiber kinking and failure.
(5) Based on the consistency in the tensile strains at crack initiation, regardless of loading type or bending degree, a strain-based failure criterion is derived, which can be applied for design purposes.
(6) The (bending) and (loading) displacement rates in both bending process and service load application do not influence the structural responses.
(7) The good agreement between experimental and numerical results confirms the effectiveness of the one- and two-step structural analysis method applied in finite element analysis.

These conclusions provide essential insights into the short-term behavior of fiber-polymer composite bending-active elastica beams and offer practical considerations for structural design in terms of material failure. However, considering the viscoelastic nature of composites, long-term effects such as creep and relaxation need to be further investigated.

CRediT authorship contribution statement

Tara Habibi: Conceptualization, Investigation, Formal analysis, Writing – original draft. **Landolf Rhode-Barbarigos:** Writing – review & editing. **Thomas Keller:** Conceptualization, Validation, Writing – review & editing, Supervision.

Declaration of competing interest

The authors declare that they have no known competing financial interests or personal relationships that could have appeared to influence the work reported in this paper.

Data availability

The raw/processed data required to reproduce these findings cannot be shared at this time as the data also forms part of an ongoing study

Acknowledgement

The authors would like to acknowledge the support of BlueOffice Architecture, Bellinzona; Azienda Multiservizi Bellinzona, Bellinzona; ass architectes associés sa, Le Lignon-Genève; ing. Lorenzo Bassi, Pregassona; Passera & Associati SA, Lugano, and Luca Loris Georges Mari, Jonathan Martin and Serge Despont for developing the experimental setup.

References

[1] Lienhard J, Knippers J. Considerations on the scaling of bending-active structures. Int J Sp Struct 2013;28(3–4):137–47. https://doi.org/10.1260/0266-3511.28.3-4.137.
[2] Habibi T, Rhode-Barbarigos L, Keller T. Fiber-polymer composites for permanent large-scale bending-active elastica beams. Compos Struct 2021;294–115809 (November):2022. https://doi.org/10.1016/j.compstruct.2022.115809.
[3] Lienhard J. Bending-Active Structures in static and kinetic systems and the structural potentials therein Form-finding strategies using elastic deformation. PhD thesis at Universität Stuttgart, 2014. doi: ISBN 973-3-922302-36-0.
[4] Kotelnikova-Weiler N, Douthe C, Hernandez EL, Baverel O, Gengnagel C, Caron J-F. Materials for actively-bent structures. Int J Sp Struct 2013;28(3–4):229–40. https://doi.org/10.1260/0266-3511.28.3-4.229.
[5] Du Peloux L, Tayeb F, Baverel O, Caron JF. Construction of a large composite gridshell structure: a lightweight structure made with pultruded glass fibre reinforced polymer tubes. Struct Eng Int 2016;26(2):160–7. https://doi.org/10.2749/101686616X14555428758885.
[6] Knippers J, Cremers J, Gabler M, Lienhard J. Construction manual for Polymers + membranes materials, semi-finished products, form finding. *Design* München: Birkhäuser 2011. https://doi.org/10.11129/detail.9783034614702.
[7] Roorda J. Stability of structures with small imperfections. J Eng Mech Div 1965;91 (1):87–106. https://doi.org/10.1061/JMCEA3.0000586.
[8] Clifton RJ. Snap-buckling of a prestressed shallow arch. Proceedings of ASCE structural and engineering mechanics division specialty conference on optimization and nonlinear problems. 1968.
[9] Huddleston JV. Behavior of a steep prestressed arch made from a buckled strut. J Appl Mech 1970;37(4):984–94. https://doi.org/10.1115/1.3408728.
[10] Keller T, Bai Y, Vallée T. Long-term performance of a glass fiber-reinforced Polymer truss bridge. J Compos Constr 2007;11(1):99–108. https://doi.org/10.1061/(ASCE)1090-0268(2007)11:1(99).
[11] Fung YC, Kaplan A. Buckling of low arches or curved beams of small curvature. Tech Rep 1952.
[12] Hoff NJ, Bruce VG. Dynamic analysis of the buckling of laterally loaded flat arches. J Math Phys 1953;32(1–4):276–88. https://doi.org/10.1002/sapm1953321276.
[13] Schreyer HL, Masur EF. Buckling of shallow arches. J Eng Mech Div 1966;92(4): 1–19. https://doi.org/10.1061/JMCEA3.0000772.
[14] Timoshenko SP, Gere JM. Theory of Elastic Stability, Second Edi, vol. Engineerin. New York: McGraw-Hill; 1985.
[15] Lo C, Conway H. The elastic stability of curved beams. Int J Mech Sci 1967;9(8): 527–38. https://doi.org/10.1016/0020-7403(67)90052-5.
[16] Huddleston JV. Finite deflections and snap-through of high Circular arches. J Appl Mech 1968;35(4):763–9. https://doi.org/10.1115/1.3601302.
[17] Huddleston JV. A Numerical technique for elastica problems. J Eng Mech Div 1968;94(5):1159–65. https://doi.org/10.1061/jmcea3.0001028.
[18] Clifton RJ. Snap-buckling of shallow prestressed arches. J Eng Mech Div 1970;96 (6):1157–70. https://doi.org/10.1061/jmcea3.0001309.
[19] Wolde-Tinsae AM, Huddleston JV. Three-dimensional stability of prestressed arches. J Eng Mech Div 1977;103(5):855–67. https://doi.org/10.1061/JMCEA3.0002278.
[20] Huddleston JV. The compressible elastica in three dimensions. Int J Mech Sci 1978; 20(4):229–36. https://doi.org/10.1016/0020-7403(78)90084-X.
[21] Wolde-Tinsae AM, Huddleston JV. Nonlinear three-dimensional analysis of prebuckled domes. Comput Struct 1981;14(3–4):215–24. https://doi.org/10.1016/0045-7949(81)90007-9.
[22] Thompson JMT, Hunt GW. On the buckling and imperfection-sensitivity of arches with and without prestress. Int J Solids Struct 1983;19(5):445–59. https://doi.org/10.1016/0020-7683(83)90055-0.
[23] Chini SA. Nonlinear stability analysis of prestressed domes using the finite element method. Md: University of Maryland, at college Prak; 1986. PhD thesis at.
[24] Chini SA, Wolde-Tinsae AM. Buckling test of prestressed arches in centrifuge. J Eng Mech 1988;114(6):1063–75. https://doi.org/10.1061/(asce)0733-9399(1988)114:6(1063).
[25] Chini SA, Wolde-Tinsae AM. Effect of prestressing on elastica arches. J Eng Mech 1988;114(10):1791–800. https://doi.org/10.1061/(ASCE)0733-9399(1988)114:10(1791).
[26] Pippard AB. The elastic arch and its modes of instability. Eur J Phys 1990;11(6): 359–65. https://doi.org/10.1088/0143-0807/11/6/008.
[27] D. Nelsen, "A feasibility study on the use of sandwich construction in prebuckled arches," PhD thesis at Iowa State University, Digital Repository, Ames, 1979. doi: 10.31274/rtd-180813-8065.
[28] Mirmiran A, Wolde-Tinsae AM. Stability of prebuckled Sandwich elastica arches: parametric study. J Eng Mech 1993;119(4):767–85. https://doi.org/10.1061/(asce)0733-9399(1993)119:4(767).
[29] Mirmiran A, Amde AM. Inelastic buckling of prestressed Sandwich or homogeneous arches. J Struct Eng 1993;119(9):2733–43. https://doi.org/10.1061/(ASCE)0733-9445(1993)119:9(2733).
[30] Mirmiran A, Amde AM. Effects of fabrication process on prestressed composite arches. J Struct Eng 1995;121(1):124–31. https://doi.org/10.1061/(asce)0733-9445(1995)121:1(124).
[31] Mirmiran A, Wolde-Tinsae AM. Buckling and postbuckling of prestressed Sandwich arches. J Struct Eng 1993;119(1):262–78. https://doi.org/10.1061/(asce)0733-9445(1993)119:1(262).
[32] Amde AM, Mirmiran A, Nelsen D. Stability tests of Sandwich composite elastica arches. J Struct Eng 2002;128(5):683–6. https://doi.org/10.1061/(asce)0733-9445(2002)128:5(683).
[33] Ragavan V, Amde AM. Nonlinear buckling and postbuckling of cable-stiffened prestressed domes. J Eng Mech 1999;125(10):1164–72. https://doi.org/10.1061/(ASCE)0733-9399(1999)125:10(1164).
[34] Ragavan V, Amde AM. Nonlinear stability of ring-stiffened prestressed domes. J Struct Eng 2000;126(7):838–43. https://doi.org/10.1061/(ASCE)0733-9445(2000)126:7(838).
[35] Mirmiran A, Amde AM, Xu Z. Effect of geometric and loading conditions on stability of prestressed arches. Int J Struct Stab Dyn 2001;01(04):509–26. https://doi.org/10.1142/S0219455401000329.
[36] Mirmiran A, Amde AM, Xu Z. Elasto-plastic buckling of prestressed arches. Int J Struct Stab Dyn 2002;02(03):295–313. https://doi.org/10.1142/S0219455402000580.
[37] L. Bouhaya, O. Baverel, and J.-F. Caron, "Mapping two-way continuous elastic grid on an imposed surface: Application to grid shells," in *Proceedings of the International Association for Shell and Spatial Structures (IASS) Symposium 2009, Valencia Evolution and Trends in Design, Analysis and Construction of Shell and Spatial Structures*, 2009, pp. 989–997. [Online]. Available: https://riunet.upv.es/handle/10251/6963.
[38] Tayeb F, Caron JF, Baverel O, Du Peloux L. Stability and robustness of a 300 m2 composite gridshell structure. Constr Build Mater 2013;49:926–38. https://doi.org/10.1016/j.conbuildmat.2013.04.036.
[39] Lefevre B, Douthe C, Baverel O. Buckling of elastic gridshells. J Int Assoc Shell Spat Struct 2015;56(3):153–71.
[40] Mesnil R, Ochsendorf J, Douthe C. Stability of pseudo-Funicular elastic grid shells. Int J Sp Struct 2015;30(1):27–36. https://doi.org/10.1260/0266-3511.30.1.27.
[41] C. Lázaro, S. Monleón, and J. Casanova, "Can the force density method be extended for active bending structures?,"in *Proceedings of the International Association for Shell and Spatial Structures (IASS), Amsterdam, Future Visions*, 2015.
[42] S. Schleicher and L. M. Riccardo, "Bending-Active Plates, Form-Finding and Form-Conversion," in *ACADIA2016*, 2016, no. October, pp. 260–269.
[43] S. Schleicher, R. La Magna, and J. Zabel, "Bending-active sandwich shells: Studio one research pavilion 2017," *Discip. Disrupt. - Proc. Cat. 37th Annu. Conf. Assoc. Comput. Aided Des. Archit. ACADIA 2017*, pp. 544–551, 2017.
[44] Sakai Y, Ohsaki M, Adriaenssens S. A 3-dimensional elastic beam model for form-finding of bending-active gridshells. Int J Solids Struct 2020;193–194:328–37. https://doi.org/10.1016/j.ijsolstr.2020.02.034.
[45] Lázaro C, Monleón S, Bessini J. Tangent stiffness in point-loaded elastica arches. In: Proceedings of the IASS Annual Symposium 2017. "Interfaces: architecture. engineering.science;" 2017, no. September.
[46] Bessini J, Monleón S, Casanova J, Lázaro C. Shape generation of bending-active braced arches based on elastica curves. J Int Assoc Shell Spat Struct 2021;62(2): 138–52. https://doi.org/10.20898/j.iass.2021.016.
[47] Fiberline, "Fiberline Composites A/S - Design Manual" 2003.
[48] "CEN/TS 19101:2022. "Design of fibre-polymer composite structures". European Committee for Standardization. CEN/TC 250; 2022.
[49] prEN 1990. Basis of structural and geotechnical design" European Committee for Standardization. CEN/TC 2021;250:2021.